JBC RESEARCH ARTICLE

A natural fusion of flavodiiron, rubredoxin, and rubredoxin oxidoreductase domains is a self-sufficient water-forming oxidase of *Trichomonas vaginalis*

Received for publication, January 26, 2022, and in revised form, June 23, 2022 Published, Papers in Press, June 30, 2022,
https://doi.org/10.1016/j.jbc.2022.102210

Evana N. Abdulaziz[1], Tristan A. Bell[2], Bazlur Rashid[3], Mina L. Heacock[1], Tarik Begic[3], Owen S. Skinner[2,4], Mohammad A. Yaseen[5], Luke H. Chao[2], Vamsi K. Mootha[2,4], Antonio J. Pierik[3], and Valentin Cracan[1,6,*]

From the [1]Redox Biology and Metabolism Laboratory, Scintillon Institute, San Diego, California, USA; [2]Department of Molecular Biology, Massachusetts General Hospital, Harvard Medical School, Boston, Massachusetts, USA; [3]Faculty of Chemistry, University of Kaiserslautern, Kaiserslautern, Germany; [4]Howard Hughes Medical Institute, Massachusetts General Hospital, Boston, Massachusetts, USA; [5]Department of Bioengineering, Northeastern University, Boston, Massachusetts, USA; [6]Department of Chemistry, The Scripps Research Institute, La Jolla, California, USA

Edited by Alex Toker

Microaerophilic pathogens such as *Giardia lamblia*, *Entamoeba histolytica*, and *Trichomonas vaginalis* have robust oxygen consumption systems to detoxify oxygen and maintain intracellular redox balance. This oxygen consumption results from H_2O-forming NADH oxidase (NOX) activity of two distinct flavin-containing systems: H_2O-forming NOXes and multicomponent flavodiiron proteins (FDPs). Neither system is membrane bound, and both recycle NADH into oxidized NAD^+ while simultaneously removing O_2 from the local environment. However, little is known about the specific contributions of these systems in *T. vaginalis*. In this study, we use bioinformatics and biochemical analyses to show that *T. vaginalis* lacks a NOX–like enzyme and instead harbors three paralogous genes (FDPF1–3), each encoding a natural fusion product between the N-terminal FDP, central rubredoxin (Rb), and C-terminal NADH:Rb oxidoreductase domains. Unlike a "stand-alone" FDP that lacks Rb and oxidoreductase domains, this natural fusion protein with fully populated flavin redox centers directly accepts reducing equivalents of NADH to catalyze the four-electron reduction of oxygen to water within a single polypeptide with an extremely high turnover. Furthermore, using single-particle cryo-EM, we present structural insights into the spatial organization of the FDP core within this multidomain fusion protein. Together, these results contribute to our understanding of systems that allow protozoan parasites to maintain optimal redox balance and survive transient exposure to oxic conditions.

Trichomonas vaginalis is a microaerophilic human protozoan parasite that causes trichomoniasis, one of the most common sexually transmitted infections (1, 2). A distinct feature of *T. vaginalis* as well as other human protozoan parasites such as *Giardia lamblia* (syn. *intestinalis*, *duodenalis*) and *Entamoeba histolytica* is their ability to tolerate low oxygen concentrations and transient exposure to oxic conditions. This is remarkable as these protozoa depend on metabolic enzymes that are extremely sensitive to oxygen, such as pyruvate:ferredoxin oxidoreductase and FeFe-hydrogenase (3, 4). Another common feature of these single-celled eukaryotic organisms is that they do not contain traditional mitochondria and instead harbor mitochondria-derived organelles called mitosomes or hydrogenosomes that lack a membrane-bound electron transport chain (ETC) to carry out oxidative phosphorylation (4). At the same time, it is well recognized that *T. vaginalis* consumes oxygen and that this oxygen consumption is insensitive to ETC inhibitors (such as cyanide or azide) (4, 5). Over the years, most of this oxygen consumption was attributed to enzymes that catalyze a conversion of diatomic oxygen to two benign water molecules at the expense of reducing equivalents of NAD(P)H (the H_2O-forming NAD(P)H oxidase reaction) (Fig. 1*A*). This reaction not only serves the "oxygen scrubbing" role, but at the same time, it maintains uninterrupted supply of oxidized NAD^+ to support an optimal intracellular NADH/NAD^+ ratio (4, 6).

We now know that two different enzymatic systems evolved to catalyze the H_2O-forming NADH oxidase (NOX) reaction in various bacteria and protozoa, most likely through convergent evolution (Fig. 1*A*). The first system is a H_2O-forming NOX that belongs to the evolutionarily versatile "two dinucleotide-binding domain" flavoproteins (tDBDF) superfamily (Fig. 1*A*) (7–9). These soluble NOXes are not related to the mammalian transmembrane reactive oxygen species (ROS)–producing NADPH oxidases (NOX1–5 and DUOX1–2) (10). The active site of a typical tDBDF superfamily NOX enzyme (~50 kDa per monomer) consists of a single FAD cofactor and an adjacent redox-active cysteine that cycles between sulfenic acid and reduced cysteine to accomplish the four electron reductions of oxygen to water (7, 11, 12). For example, in a previous study, we performed extensive biochemical and structural characterization of a water-forming NOX from *Lactobacillus brevis* (*Lb*NOX) (12). *Lb*NOX proved

* For correspondence: Valentin Cracan, vcracan@scripps.edu.
Present address for Evana N. Abdulaziz: CW Associate Scientist, Amgen, Thousand Oaks, California, 91320, USA.

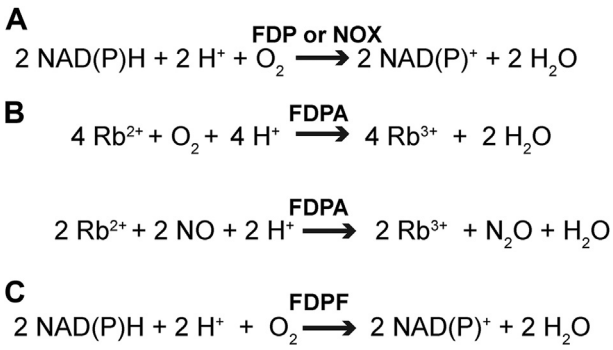

Figure 1. Reactions catalyzed by class A and class F flavodiiron proteins (FDPA and FDPF) as well as by a H_2O-forming NADH oxidase (NOX). *A*, the net H_2O-forming NAD(P)H oxidase reaction catalyzed by a multicomponent FDP-based system or a H_2O-forming NOX. *B*, in the simplest configuration, FDPA receives electrons from reduced rubredoxin (Rb). Some FDPAs can also reduce nitric oxide to nitrous oxide and water, respectively. *C*, FDPF represents a natural fusion, where the FDP core protein is fused with both Rb and NADH:Rb oxidoreductase (NROR) redox partners.

to be an extremely efficient enzyme with strict specificity toward NADH, with K_ms for O_2 and NADH, of ∼2 μM and 69 ± 3 μM, respectively, and a turnover number of 648 ± 28 s^{-1} while less than 2% of input electrons leads to off-target H_2O_2 formation (12).

Flavodiiron protein (FDP) is a second system with H_2O-forming oxidase activity (Figs. 1, *A*–*C* and 2*A*). Interestingly, some FDPs can also use nitric oxide (NO) gas as a substrate or can have mixed O_2/NO specificity (Fig. 1*B*) (13–16). The minimal unit of a typical FDP (in the new classification class A FDP [FDPA], see later) is a ∼50 kDa protein with two subdomains: an N-terminal metallo-β-lactamase–like subdomain containing the dinuclear Fe–Fe center (diiron center) and a C-terminal subdomain, containing the FMN redox cofactor (16–18)(Fig. 2*A*). Within a monomer, the distance between the oxygen-binding diiron center and the FMN plane is approximately 40 Å in all reported structures of FDPs, much greater than the ∼15 Å maximum distance that allows efficient electron transfer (ET) (19). As such, the functional unit of a "stand-alone" FDPA is comprised of a "head-to-tail" homodimer that positions the diiron center of one protomer adjacent to the FMN bound of its neighboring protomer (16, 18, 20). Another major difference between NOX and FDP enzymes is that the latter cannot directly receive electrons from NAD(P)H and requires additional protein adaptors as substrates. At the same time, FDPs can directly receive electrons from rubredoxin (Rb), a ∼6 kDa protein that contains an $Fe(SCys)_4$ center and which in bacteria and *Archaea* is reduced by a dedicated NAD(P)H:Rb oxidoreductase (NROR) or similar systems (4, 21–25) (Fig. 1*B*). Notably, in biochemical and spectroscopic studies of previously characterized FDPAs, only artificial protein substrates were used (*i.e.*, recombinant NADH:flavorubredoxin oxidoreductase and a truncated Rb domain of flavorubredoxin, both from *Escherichia coli*) as in the corresponding organisms, the natural electron donors of FDPs were not identified (17, 26, 27).

Recent bioinformatics analysis revealed that in many organisms, FDPs are naturally fused to various redox partners and led to the current classification of this large group of proteins (26–28). According to this classification "stand-alone" FDPs that contain only diiron and FMN centers are designated as FDPAs (26) (Fig. 2*A*). Several additional classes were proposed for proteins in which one or more other domains are fused genetically to the C-terminal side of the FDP core (classes B to H) (26). These additional redox centers may play crucial roles in dedicated ET pathways, through which reducing equivalents of NAD(P)H or other substrates are relayed to the gas-binding diiron site (26).

We turned our attention to the water-forming oxidase activity ascribed to *T. vaginalis* because our laboratory is interested in oxygen-metabolizing systems that allow unicellular organisms that lack an ETC to maintain an optimal redox environment (12). While *T. vaginalis* as well *G. lamblia* and *E. histolytica* contain biochemically verified class A FDPs (FDPAs), there is still confusion in the literature about a NOX-like enzyme in this organism (20, 29, 30). The first attempt to purify the H_2O-forming NOX activity from *T. vaginalis* resulted in an isolate that was active only with NADH (no activity with NADPH was detected) with a specific activity of

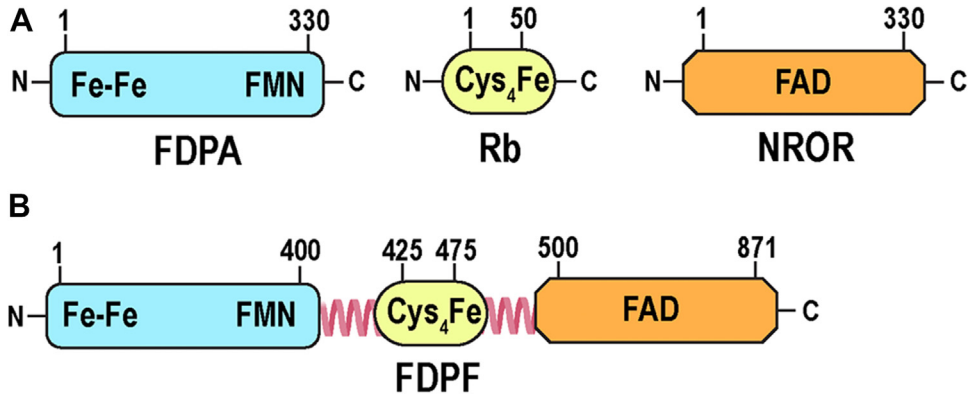

Figure 2. Domain organization of class A and class F flavodiiron proteins (FDPA and FDPF). *A*, FDPA contains the diiron center (Fe–Fe) and a flavin cofactor (FMN) (depicted in *light blue*). Two additional redox partners of a "stand-alone" FDPA are: (i) rubredoxin (Rb) (depicted in *yellow*) and (ii) NADH:Rb oxidoreductase (NROR) (depicted in *orange*) (Fig. 1). The $Fe(SCys)_4$ center of Rb is formed by a central iron, which is coordinated by four cysteines. The redox center of NROR contains a flavin redox cofactor (FAD). *B*, FDPF represents a natural fusion between the N-terminal FDP core, Rb-like domain, and NROR-like domain. Loops connecting the middle Rb-like domain with the N-terminal FDP core and the NROR domain are shown.

16.5 μmol min^{-1} mg^{-1} and K_m for NADH of 7.4 μM (31). The authors reported that the preparation consumed NADH and O_2 with 2:1 stoichiometry and did not produce H_2O_2 as a byproduct. Unfortunately, neither the N-terminal sequence nor the molecular mass of the enzyme was reported at that time. In a later study, a H_2O-forming NOX activity from *T. vaginalis* was purified and exhibited a k_{cat} of 470 s^{-1} and K_m for NADH of 5.4 μM (32). Interestingly, in that study, when the H_2O-forming NOX preparation was analyzed by SDS-PAGE, it migrated as two closely spaced unusually high molecular mass bands of 97 to 97.5 kDa. The latter observation was inconsistent with a NOX protein, which is usually ∼50 kDa (see previous one) (31–34).

In this study, using bioinformatics analysis, we show that the genome of *T. vaginalis* does not possess a typical tDBDF superfamily *nox* gene but instead harbors three genes that encode a natural fusion between flavodiiron, Rb, and NROR domains (class F FDP [FDPF] according to the new classification) (Fig. 2*B*) (26). We provide initial biochemical characterization of these three recombinant FDPFs from *T. vaginalis* (*Tv*FDPF1–3). Furthermore, we focus our biochemical and biophysical characterization on *Tv*FDPF3, as it is the most active and well-behaved enzyme. Together, our results demonstrate that natural fusion protein *Tv*FDPF3 allows the crosstalk of all three domains, ultimately relaying electrons from NADH to O_2. We also employ single-particle cryo-EM to visualize the dimerization interface of *Tv*FDPF3. Our observations suggest that the enzymatic activity described by Tanabe in 1979 and by Bradley and Linstead in 1988 was misassigned as a NOX-like enzyme and that it is in fact an FDPF. Together, our biochemical, spectroscopic, and structural studies provide important new insights into how the FDPF system from *T. vaginalis* achieves extremely efficient H_2O-forming oxidase activity using four separate redox centers.

Results

Identification of FDPFs as enzyme candidates for previously reported H_2O-forming NOX activity in T. vaginalis

Because we were interested in evolutionary innovations that allow lower organisms that lack a membrane-bound ETC to maintain an optimal intracellular redox environment, we explored NOXes ascribed to human protozoan parasites (4). While we easily identified previously characterized NOX in the genome of *G. lamblia* (33–35), the closest matches in the genome of *T. vaginalis* were three proteins, all of which were 871 amino acids in length and annotated in the EuPathDB database for human protozoan parasites as "pyridine nucleotide–disulfide oxidoreductase" or "apoptosis-inducing factor" (TVAG_263800, TVAG_049830, and TVAG_121610) (Table S1). We noticed that each of these three proteins is a fusion containing an N-terminal FDP domain, a central Rb domain, and a C-terminal NROR domain (Fig. 2*B*). Based on the recent classification, all these three fusion proteins in *T. vaginalis* are FDPFs (from now on, we denote them as *Tv*FDPF1–3) (26) (Fig. 2*B*).

When compared with stand-alone FDPAs from *T. vaginalis*, *G. lamblia*, and several other organisms, the N-terminal FDP domain of *Tv*FDPF1–3 includes the previously recognized canonical sequences containing the ligands of the diiron center: Fe 1 (His82-X-Glu84-X-Asp86-His87, *Tv*FDPF3 numbering) and Fe 2 (His148-X_{18}-Asp166-X_{64}-His230) (Fig. S1). The middle domain of *Tv*FDPF1–3 is homologous to Rbs and the C-terminal domain of bacterial rubrerythrin (Fig. S2). A central feature of the middle domain of *Tv*FDPF1–3 is the presence of two pairs of Cys-X_2-Cys sequence patterns that coordinate the iron of the $Fe(SCys)_4$ center. This middle Rb-like domain is flanked at both sides by less conserved ∼25 to 30 amino acid linkers. The C-terminal domain of *Tv*FDPF1–3 is homologous to previously described stand-alone NRORs (36, 37). These proteins are using NADH to reduce the FAD cofactor, which subsequently donates electrons to the Rb or similar redox partners (36, 37). We note that both the GxGxxG dinucleotide–binding motif and the NAD(P)H substrate specificity loop are identifiable in the C-terminal NROR domain of *Tv*FDPF1–3 as well as in other closely related members of the tDBDF superfamily, including a "stand-alone" NROR, NADH:ferredoxin oxidoreductase, and CoA-disulfide reductase (Fig. S3). Because both NRORs and NOXes belong to the tDBDF superfamily of flavoenzymes, our initial BLAST analysis identified *Tv*FDPF1–3 as the closest NOX homologs (*i.e.*, the C-terminal domain of FDPFs [*i.e.*, NROR] is homologous to NOX) (Fig. S3) (9).

Cloning and initial purification of class F fusion FDPs from T. vaginalis *(Tv*FDPF1–3*)*

To test whether *Tv*FDPF1–3 exhibit the H_2O-forming oxidase activity and accept electrons directly from NADH or NADPH, the corresponding genes from *T. vaginalis* were cloned with a C-terminal hexa-histidine tag into a bacterial expression vector. All three genes had no introns, as it is common in *T. vaginalis*, *G. lamblia*, and other parasitic protozoa. When purified, all three recombinant proteins were brown in color and migrated as ∼100 kDa band as judged by the SDS-PAGE analysis (Figs. S4, *A*–*C* and S5). Notably, the *Tv*FDPF2 protein was prone to severe aggregation, and during purification, the protein eluted in the void volume of the size-exclusion column. Based on analytical gel filtration and assuming a globular shape, we estimated an apparent molecular weight for *Tv*FDPF1 of 272 ± 7 kDa and for *Tv*FDPF3 of 289 ± 3 kDa. The absorption spectra of all three oxidized proteins had composite features resulting from a sum of flavin bands (contributing at 350–500 nm) and an $Fe(SCys)_4$ center of Rb (contributing at 373 nm and above 500 nm) with maxima at 379, 454, 475, and 568 nm for *Tv*FDPF1; 374, 451, 478, and 565 nm for *Tv*FDPF2; and 378, 451, 475, and 574 nm for *Tv*FDPF3 (Figs. S4, *B* and *C* and S5). In the presence of excess sodium dithionite, these cofactors were reduced, and the visible absorbance was almost completely bleached (Figs. S4, *B* and *C* and S5).

We next employed LC–MS to determine both the molecular identity and quantity of flavin cofactors bound to *Tv*FDPF1–3. While we unambiguously identified both FAD and FMN

within *Tv*FDPF1–3, the actual stoichiometries of these cofactors per protein monomer were drastically different (Table 1). Both *Tv*FDPF1 and *Tv*FDPF3 had full occupancy with FAD per monomer (1.02 ± 0.05 and 1.00 ± 0.12, respectively). However, FMN was present only at 0.010 ± 0.004 occupancy per monomer (∼1%) in *Tv*FDPF1 and 0.090 ± 0.006 (∼9%) in *Tv*FDPF3 (Table 1). *Tv*FDPF2 had poor occupancy of both FAD and FMN, which is not surprising given its poor behavior during purification. Thus far, only the FMN cofactor was reported in FDPAs, and it seemed logical that poor occupancy of FMN in our preparations of *Tv*FDPF1–3 reflected occupancy of the N-terminal FDP domain only. Direct addition of 300 μM FMN to the lysis buffer during purification of *Tv*FDPF1 did not improve FMN occupancy (Table 1).

Because Fe is a part of both the diiron center and the Rb-like domain, we measured iron content of all three proteins (Table S2). We found that despite addition of Mohr's salt (ammonium iron(II) sulfate) during protein expression, all purified *Tv*FDPF1–3 had substoichiometric iron occupancy (3 Fe per monomer is expected). The highest Fe occupancy of 0.82 ± 0.17 was observed for *Tv*FDPF1, whereas *Tv*FDPF2 and *Tv*FDPF3 had 0.41 ± 0.02 and 0.58 ± 0.10, respectively (Table S2).

Specificity of Tv*FDPF1–3 toward NADH and NADPH*

Because previously reported H_2O-forming NOX-like activities purified from *T. vaginalis* were tested with both NADH and NADPH, we tested consumption of both redox cofactors in our enzymatic assays (Table 2 and Fig. S4, *D–F*). Michaelis–Menten analysis of the reaction catalyzed by *Tv*FDPF1–3 indicates that NADH is the preferred substrate over NADPH for all three enzymes. The highest V_{max} of 12 ± 1 μmol min^{-1} mg^{-1} at 37 °C was observed for *Tv*FDPF3. We found that the lowest K_m for NADH among all variants was 2.9 ± 0.8 μM for *Tv*FDPF1. This value is in sharp contrast to the K_m for NADH of *Tv*FDPF3 that was 40 ± 8 μM. However, because V_{max} for *Tv*FDPF1 was low, the overall catalytic efficiency k_{cat}/K_m of both *Tv*FDPF1 and *Tv*FDPF3 as well of *Tv*FDPF2 with NADH was very similar. Michaelis–Menten fitting of the NADPH data results in K_m values in the millimolar range, far above its physiological concentration (Table 2). Our results clearly support our prediction that the fusion FDPF from *T. vaginalis* is a "self-sufficient" enzyme that directly accepts reducing equivalents from NAD(P)H. Because *Tv*FDPF2 had low yield and was not stable, we focused further kinetic studies on *Tv*FDPF1 and *Tv*FDPF3. We also determined that *Tv*FDPF3 had little activity with NO (<2% when compared with the NADH to O_2 activity, Fig. S6).

Table 1
FAD and FMN quantification

Protein	FAD per protein monomer	FMN per protein monomer
*Tv*FDPF1	1.02 ± 0.05	0.010 ± 0.004
*Tv*FDPF1[a]	1.12 ± 0.08	0.010 ± 0.004
*Tv*FDPF2	0.32 ± 0.05	0.009 ± 0.002
*Tv*FDPF3	1.00 ± 0.12	0.090 ± 0.006
holo*Tv*FDPF3	0.94 ± 0.09	0.92 ± 0.09

Cofactors were quantified using LC–MS as described under the "Experimental procedures" section. Stoichiometry was calculated per protein monomer. Data represent (n = 4–6) independent experiments ± SD. "Holo" refers to highly active *Tv*FDPF3 fully loaded with FAD and FMN cofactors.
[a] 0.3 mM FMN was added to the lysis buffer during purification.

Kinetics of oxygen consumption and H_2O_2 production

We next studied the reaction catalyzed by *Tv*FDPF1 and 3, by monitoring both NADH and oxygen consumption simultaneously (Fig. S7, *A* and *B*). To our surprise, there was a clear difference in NADH-to-O_2 stoichiometry for *Tv*FDPF1 when compared with *Tv*FDPF3. With *Tv*FDPF3, two consecutive additions of 250 μM NADH were needed to completely reduce O_2 of air-saturated buffer (∼250 μM) to water. In contrast, O_2 and NADH consumption by *Tv*FDPF1 had a 1:1 stoichiometry. The observed reaction traces support a H_2O-forming reaction for *Tv*FDPF3 but not for *Tv*FDPF1 preparations (low in FMN content) (Table 1). We tested this hypothesis by measuring H_2O_2 produced by either *Tv*FDPF1 or *Tv*FDPF3 with Amplex Red in a discontinuous assay (Table S3). We found that *Tv*FDPF1 produces 86 ± 5% H_2O_2, whereas *Tv*FDPF3 produces only 9.6 ± 3.7%.

*Purification of highly active holo*Tv*FDPF3*

We noticed that a minor peak but with extremely high specific activity eluted in the wash during the anion exchange purification step of *Tv*FDPF3. After modifying our purification scheme, we were able to significantly enrich and better separate this *Tv*FDPF3 fraction, which had near-stoichiometric FAD and FMN occupancy (0.94 ± 0.09 and 0.92 ± 0.09) (Table 1 and Fig. 3*A*). The apparent molecular mass of such preparations, to which we refer to as "holo*Tv*FDPF3," was 241 ± 1 kDa, as judged by analytical gel filtration (with a sharper appearance compared with both *Tv*FDPF1 and 3). We used blue native PAGE (BN-PAGE) as an independent method to assess the molecular weight of holo*Tv*FDPF3 and observed an apparent molecular mass of 322 ± 24 kDa (Fig. S8).

The absorption spectrum of holo*Tv*FDPF3 had stronger features of flavin bands at 375, 451, and 472 nm as well as of the Rb-like center at 566 nm (Fig. 3*B*). Most importantly, the Michaelis–Menten analysis revealed that the V_{max} of holo*Tv*FDPF3 was 291 ± 26 μmol min^{-1} mg^{-1}, a significant increase (∼24 times) compared with the low FMN occupancy *Tv*FDPF3. The K_ms for NADH and NADPH were 56 ± 2 μM and 427 ± 160 μM, respectively, and k_{cat} (with NADH) was 466 ± 42 s^{-1} per monomer (Table 2 and Fig. 3*C*). The iron content of holo*Tv*FDPF3 was 1.70 ± 0.12, which is three times higher compared with initially purified low-activity *Tv*FDPF3 (Table S2). We also used inductively coupled plasma mass spectrometry (ICP-MS) to characterize the metal content of holo*Tv*FDPF3 and detected a small amount of Zn^{2+} that is likely incorporated in place of $Fe^{2+/3+}$ in the diiron site (Table S4). Other metal ions were present only in negligible quantities. Finally, the H_2O_2 byproduct formation was twofold lower (5.0 ± 2.7%) than of initially purified *Tv*FDPF3 (Table S3). In summary, holo*Tv*FDPF3 had more complete FAD/FMN/Fe occupancy, as reflected in its increased specific

Table 2
Steady-state kinetic parameters of the enzymatic reactions catalyzed by *Tv*FDPF1–3 and holo*Tv*FDPF3

Protein	Substrate	K_m (μM)	V_{max} (μmol min^{-1} mg^{-1})	k_{cat} (s^{-1})	k_{cat}/K_m (s^{-1} M^{-1})
*Tv*FDPF1	NADH	2.9 ± 0.8	4.9 ± 1.2	7.8 ± 1.9	(2.6 ± 0.9) × 10^6
	NADPH	1475 ± 486	4.9 ± 2.1	7.8 ± 3.3	(5.2 ± 2.8) × 10^3
*Tv*FDPF2	NADH	18 ± 2	6.1 ± 0.2	9.6 ± 0.3	(5.3 ± 0.6) × 10^5
	NADPH	1171 ± 208	1.1 ± 0.2	1.7 ± 0.3	(1.4 ± 0.3) × 10^3
*Tv*FDPF3	NADH	40 ± 8	12 ± 1	19 ± 2	(4.8 ± 1.0) × 10^5
	NADPH	399 ± 8	4.0 ± 0.1	6.4 ± 0.2	(1.6 ± 0.0) × 10^4
*holoTv*FDPF3	NADH	56 ± 2	291 ± 26	466 ± 42	(8.3 ± 0.8) × 10^6
	NADPH	427 ± 160	11 ± 4	18 ± 6	(4.1 ± 2.1) × 10^4

Activities were measured as described under the "Experimental procedures" section. Kinetic parameters represent the average of (n = 4–8) independent experiments ± SD. k_{cat} values were calculated per monomer.

activity, and we employed it in all our subsequent experiments (except for the experiments when *Tv*FDPF3 with a low FMN load was needed).

Titration of dithionite-reduced Tv*FDPF3 with NAD*$^+$

To directly demonstrate the entry point of reducing equivalents into *Tv*FDPF3, we performed anaerobic titration with NAD$^+$ after initial reduction with dithionite of holo*Tv*FDPF3 or a preparation of the latter with a low FMN content. Oxidized NAD$^+$ addition caused the appearance of a long wavelength band centered at 704 nm (Fig. 3*D*). This broad band reflects stacking of $FADH_2$ and NAD$^+$ planes (charge transfer complex) (37, 38). This absorbance change is complete at 1.01 ± 0.08 equivalent of NAD$^+$ per holo*Tv*FDPF3 monomer (each monomer of *Tv*FDPF3 contains one FAD and one FMN). The binding of NAD$^+$ to $FADH_2$ occurs with an estimated K_D of 0.13 μM. The same experiment with *Tv*FDPF3 almost devoid of FMN (deFMN-*Tv*FDPF3, 0.1 FMN/FAD) showed the same 704 nm band, which appeared with a stoichiometry of 1.01 ± 0.08 equivalent NAD$^+$/FAD (Fig. 3*E*). This clearly shows that although both flavins in the protein can be chemically reduced by dithionite, only FAD binds NAD$^+$ tightly. Since FMN of the FDPAs is not reduced by NADH, the observed behavior is consistent with the entry of reducing equivalents of NADH *via* $FADH_2$/FAD of the C-terminal NROR domain.

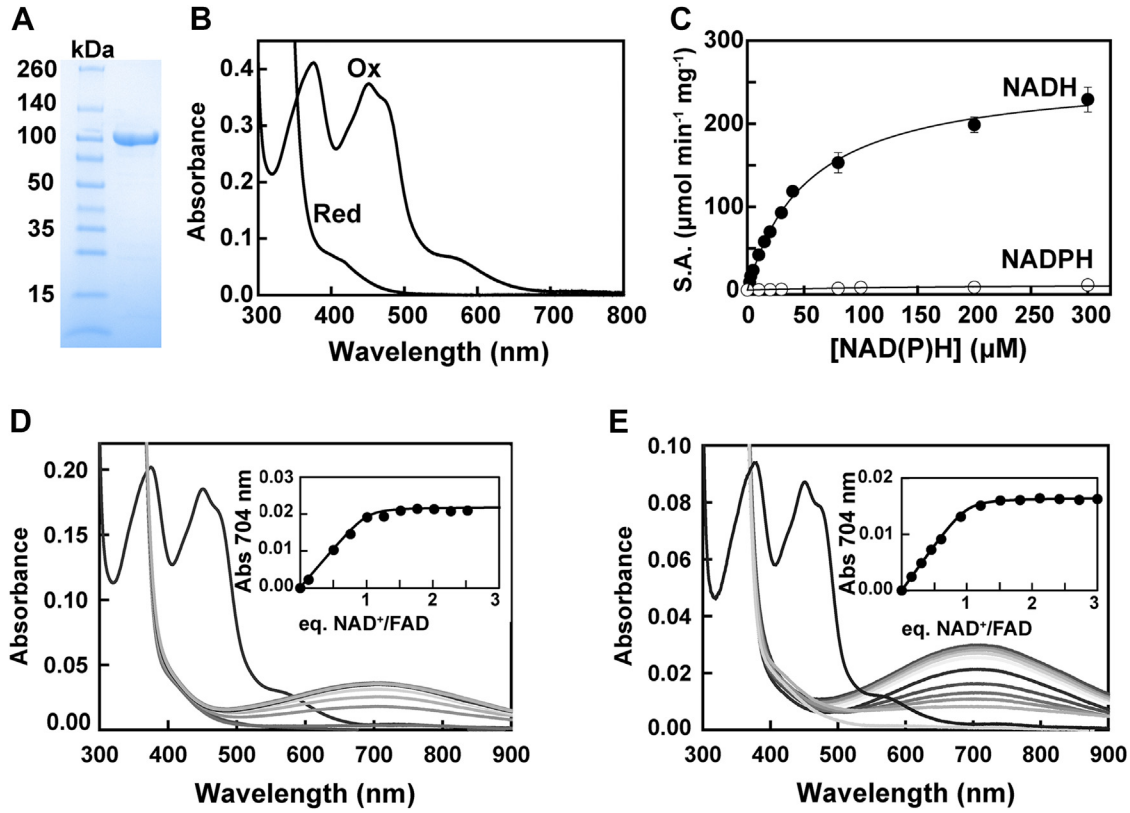

Figure 3. Biochemical and spectroscopic properties of highly active holo*Tv*FDPF3. *A*, purified holo*Tv*FDPF3 (10 μg). *B*, UV–visible spectra of holo*Tv*FDPF3 as purified. Protein was in buffer E at 20 μM (calculated based on the molecular weight of a monomer) as purified (oxidation) and after addition of 1 mM of sodium dithionite (reduction) under aerobic conditions. *C*, Michaelis–Menten analysis of the oxidase activity of holo*Tv*FDPF3 as described under the "Experimental procedures" section with NADH (*filled circles*) and NADPH (*open circles*). All kinetic parameters are summarized in Table 2. Titration of dithionite-reduced holo*Tv*FDPF3 (*D*) or deFMN-*Tv*FDPF3 (*E*) with NAD$^+$ under anaerobic conditions. Spectra shown represent the starting oxidized enzyme, the dithionite-reduced enzyme, and the reduced enzyme plus 0.1 to 3.0 equivalents of NAD$^+$/FAD. The *inset* shows the absorbance change at 704 nm *versus* equivalents of NAD$^+$/FAD. *Tv*FDPF3, FDPF3 from *Trichomonas vaginalis*.

Insights into redox centers of Tv*FDPF3 by electron paramagnetic resonance spectroscopy*

The architecture of the fusion FDP system presents a unique opportunity to biophysically characterize redox centers that are amenable to electron paramagnetic resonance (EPR) spectroscopy. FAD and FMN absorption in the visible region overwhelm the moderate absorption of the Rb center, whereas the diiron center does not absorb in the UV–visible range. On the other hand, oxidized and fully reduced flavins are diamagnetic and thus invisible by EPR. In frozen samples at low temperature signals of semiquinone, radicals can be detected but are saturated at the microwave power used and do not overlap. Thus, in the "as-isolated" holo*Tv*FDPF3 protein, a very strong isotropic EPR signal at g = 4.3 could easily be detected (Fig. 4*A*). This signal is typical for the oxidized Rb-like center, of which the d^5 ferric ion is in a high spin state (S = 5/2). Such high-spin ferric species exhibit three EPR signals from its Kramers' doublets, of which only the |±3/2> doublet shows an intense signal. Three almost identical g values at 4.3 occur if the ratio of the spin Hamiltonian parameters E and D is above 0.3 (|E/D|>0.3). Weak signals of the two other doublets (*i.e.*, only the absorption-shaped signal corresponding to the highest g value) could also be detected. The intensity of the temperature corrected g = 9.3 EPR signal of the |±1/2> doublet decreased above 4 K, indicating D = +(1.3 ± 0.6) cm^{-1} (Fig. 4*B*). In the 15 K minus 9 K difference EPR spectrum, the g = 9.8 EPR feature of the |±5/2> doublet could be revealed. For the determination of the redox midpoint potential at room temperature, holoTvFDPF3 was oxidatively and reductively titrated in the presence of organic dyes by addition of potassium ferricyanide or sodium dithionite, respectively. When such samples were frozen in liquid nitrogen, the intensity of the g = 4.3 EPR signal of the ferric state decreased upon reduction, in agreement with conversion to the EPR silent S = 2 ferrous state of the Rb-like center (Fig. 4*C*). By fitting the intensity to the appropriate Nernst equation for a single electron process, a midpoint potential of –(56 ± 10) mV *versus* H_2/H^+ for the Rb-like center was determined (Figs. 5*A* and S9).

The EPR detection of the diiron center and therefore the analysis of its redox chemistry is inherently more difficult. First, the diferrous and diferric states are diamagnetic or have integer spin and are not (easily) detectable. Detection of the mixed-valence dinuclear center (Fe^{2+}–Fe^{3+}) is hampered by the narrow temperature range at which the extremely anisotropic and large linewidth S = 1/2 EPR signal can be detected. But at moderate microwave power at 7.5 K and by combining several preparations of holo*Tv*FDPF3, we could detect a rhombic signal with g = 1.94, 1.79, and 1.53 in a sample titrated to a solution potential of +115 mV followed by addition of menadiol (Fig. 4*C*). Menadiol (reduced menadione) was previously used to characterize the EPR spectrum of an FDPF from *Clostridium difficile* by Folgosa *et al.* (39). Because of the small quantity of the high-activity *holo* enzyme and the weak EPR intensity, it was not feasible to perform extensive redox titrations as in case of the Rb-like center. By combining three high-activity preparations, dye-mediated titrations with a total number of seven datapoints enabled us to follow the EPR intensity of the mixed-valence EPR signal as a function of the solution potential. The diferric to mixed-valence potential was determined being +(55 ± 30) mV (Fig. 5*B*). Line shape changes, possibly because of reduction of the nearby FMN or conformational changes, only allowed us to estimate the mixed

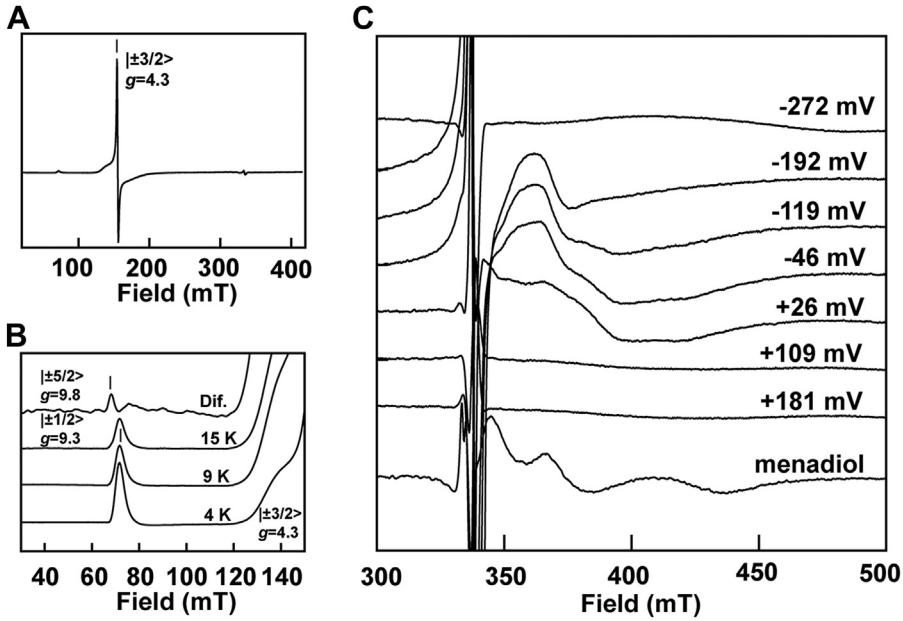

Figure 4. EPR analysis of holo*Tv*FDPF3. Spectra of the ferric rubredoxin site in the as-isolated enzyme at 15 K (*A*) or at indicated temperatures (including a 15 K minus 9 K difference spectrum) (*B*). *C*, spectra recorded at 7.5 K for samples poised at the indicated redox potentials (*versus* H_2/H^+ at pH 7.5) or poised at +115 mV and treated with 50 μM menadiol (all spectra were recorded at X-band, microwave frequency = 9.358 ± 0.003 GHz; modulation frequency = 100 kHz; modulation amplitude =1.5 mT; and microwave power = 2 mW) as described under the "Experimental procedures" section. EPR, electron paramagnetic resonance; *Tv*FDPF3, FDPF3 from *Trichomonas vaginalis*.

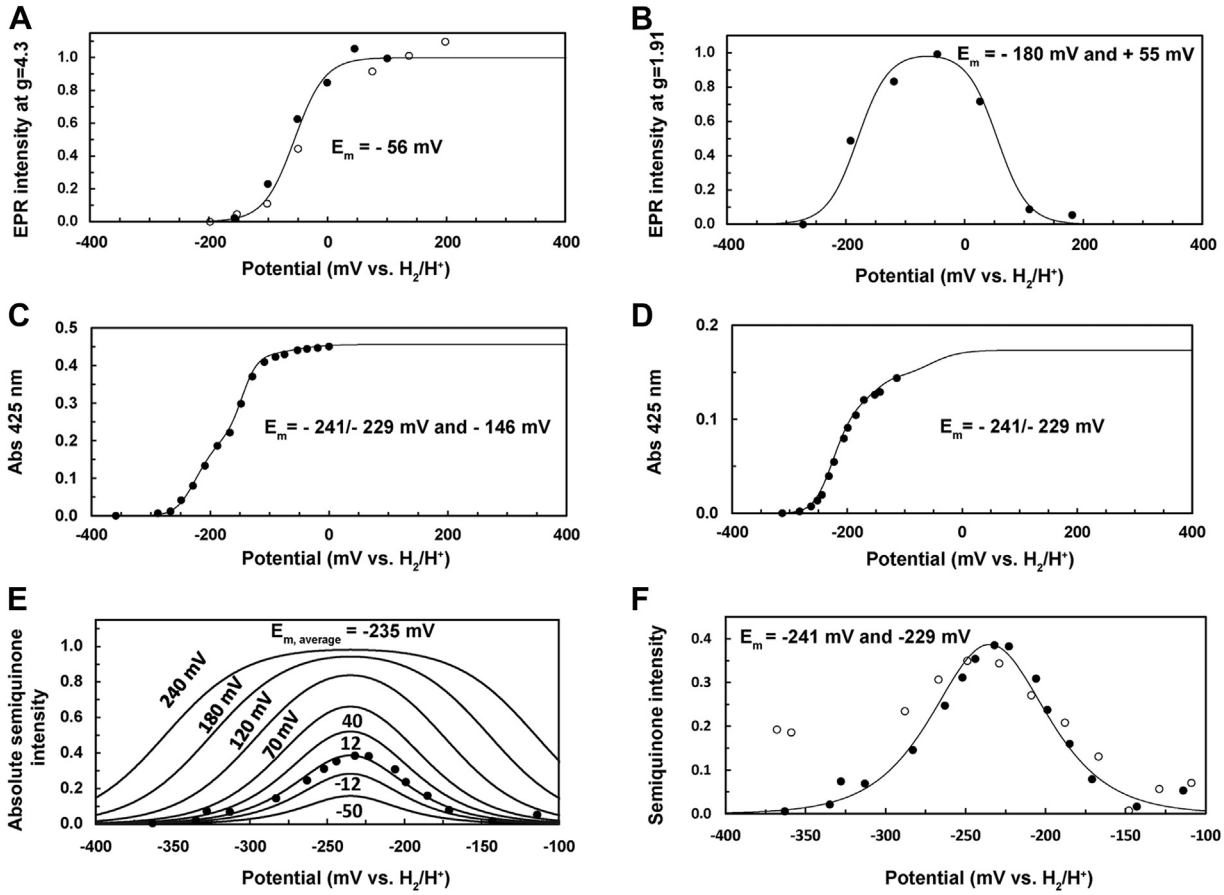

Figure 5. Determination of redox potentials of cofactors in holo*Tv*FDPF3 and deFMN-*Tv*FDPF3. *A* and *B*, EPR detected dye-mediated redox titration of holo*Tv*FDPF3 samples poised at indicated potentials and frozen in liquid nitrogen. *A*, intensities of the $g = 4.3$ EPR signal (recorded at 77 K) of the rubredoxin (Rb) site in frozen samples (*open and closed symbols* refer to two separate titrations). *B*, intensity of the mixed-valence EPR signal (amplitude at $g = 1.91$) of the dinuclear iron center. EPR conditions as in Figure 4. *C* and *D*, absorbance at 425 nm (corrected for contribution of the mediator cocktail in a parallel titration) reporting mainly on the presence of the oxidized flavin cofactors at room temperature. Fits to the (sum of) Nernst equation(s) are shown: Rb site $E_m = -56$ mV (n = 1) (*A*), FAD, $E_m = -241$ mV (n = 1) and −229 mV (n = 1), FMN, $E_m = -146$ mV (n = 2), flavins each with a 0.215 absorbance plus an absorbance of 0.026 for the Rb site ($E_m = -56$ mV, n = 1) for holo*Tv*FDPF3 in (*C*) and for deFMN-*Tv*FDPF3 with an absorbance of 0.130 for FAD, 0.016 for FMN, and 0.017 for the Rb site in (*D*). *E*, representative semiquinone titration curves for indicated separations of the $FADH_2/FADH^{\bullet}$ and $FADH^{\bullet}/FAD$ redox potentials. Experimental datapoints for deFMN-*Tv*FDPF3 are shown. *E* aand *F*, the absorbance at 600 nm minus 650 nm for the neutral semiquinone of the FAD of the titrations in (*C* and *D*) is shown. *E*, only deFMN-*Tv*FDPF3 is shown for clarity. *F*, *closed symbols* depict deFMN-*Tv*FDPF3, *open symbols* depict holo*Tv*FDPF3. The semiquinone content per FAD was calculated from the maximal absorbance at −235 mV and ε_{600} nm of 2.8 mM^{-1} cm^{-1} (41). EPR, electron paramagnetic resonance; *Tv*FDPF3, FDPF3 from *Trichomonas vaginalis*.

valence to diferrous state midpoint potential to −(180 ± 50) mV (Fig. 5*B*).

Redox titration of Tv*FDPF3 followed by UV–visible spectroscopy*

To complete our characterization of the redox chemistry of holo*Tv*FDPF3 and deFMN-*Tv*FDPF3, visible spectroscopy at room temperature was employed to estimate the midpoint potentials of FAD and FMN in the presence of 5 μM mediator concentrations in a reductive titration. Flavin-visible spectra of the protein bleached because of reduction to the hydroquinone states before onset of strongly absorbing viologen signals. At a wavelength of 425 nm, the contribution of the mediators was relatively low and constant. After spectral subtraction, the intensity of the sum of FMN- and FAD-visible contributions could be followed (Figs. 5*C* and S10*A*). Two separate redox potential ranges with 425 nm absorbance changes were observed, which based on the nearly stoichiometric presence of FMN and FAD likely correspond to redox transitions of the individual flavins. The best fit to the experimental data required an average potential of −235 ± 10 mV *versus* H_2/H^+ (pH 7.5) for the two (n = 1) transitions at low potential (Fig. 5*C*). The flavin redox change at higher potential behaved like an (n = 2) redox system with −146 ± 10 mV *versus* H_2/H^+ (pH 7.5), that is, extensive disproportionation of the semiquinone. To determine which redox transition corresponds to FAD or FMN, we performed a titration of deFMN-*Tv*FDPF3 (Figs. 5*D* and S10*B*). The redox transition of FAD at 425 nm (>90% in comparison to FMN) could be simulated with a redox potential of −235 ± 10 mV, which clearly pointed out that FAD in holo*Tv*FDPF3 has a lower potential in comparison to FMN. The low FMN content allowed a much better resolution of visible features, especially after subtraction of reference spectra of the mediator cocktail at comparable redox potentials (Fig. S10, *A* and *B*). A neutral semiquinone was

detected from its characteristic visible absorbance spectrum between 500 and 700 nm, exactly at redox potentials near the average midpoint potential of FAD/$FADH_2$ (Fig. S11*A*) (40–42). Since the shape of the normalized semiquinone intensity below a separation of 60 mV for the $FADH_2$/$FADH^{\bullet}$ and $FADH^{\bullet}$/FAD redox potentials cannot reveal an accurate value (Fig. S11*B*), we used the maximal semiquinone content per FAD of ∼0.4 to calculate a separation of approximately 12 mV (Figs. 5*E* and S11*C*). For deFMN-*Tv*FDPF3, an excellent fit to the data could be obtained with −241 ± 10 mV for $FADH_2$/$FADH^{\bullet}$ and −229 ± 10 mV for $FADH^{\bullet}$/FAD (Fig. 5*F*) using the separation of potentials from the maximal semiquinone content and experimentally determined average redox potential of −235 ± 10 mV (Fig. 5, *C* and *D*). The FAD semiquinone in holo*Tv*FDPF3 was also detected at redox potentials in the same redox potential range (Fig. 5*F*). Thus, both from NAD^+ and UV–visible redox titrations, we can unequivocally assign FAD as the low-potential entrance into the ET path of *Tv*FDPF3.

In summary, electrons within the multidomain system of *Tv*FDPF3 flow from NADH/NAD^+ (−335 mV at pH 7.5) to FAD (−235 mV), Rb (−56 mV), FMN (−146 mV), and ultimately on the dinuclear center (−180 and +55 mV, average −63 mV), the later one, in its reduced state, reacts with dioxygen. We assume that the strong electrochemical driving force from NADH and $FADH_2$ pushes the two times one ET from the Rb-like center to the FMN within the FDP domain (see Discussion later).

*Molecular architecture of holo*Tv*FDPF3 determined by cryo-EM*

We used single-particle cryo-EM to investigate domain organization and redox center positioning in holo*Tv*FDPF3. Two-dimensional class averages had clear secondary structure and were approximately 80 to 100 Å in diameter, consistent with the expected size of a globular monomer or a portion of a higher oligomer (Fig. 6*A*). Three-dimensional reconstruction of the particle set without symmetry enforced produced a

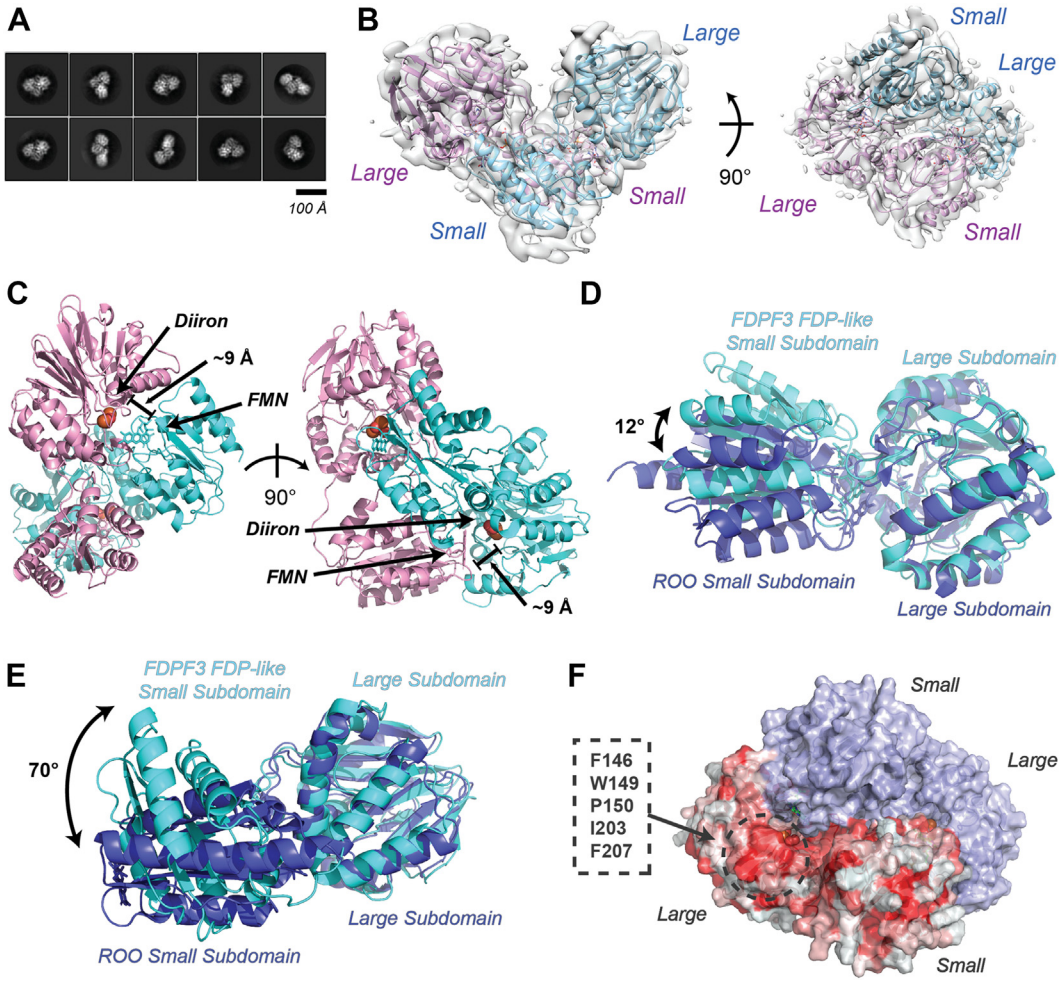

Figure 6. Cryo-EM structure of the FDP-like core of the full-length *Tv*FDPF3. *A*, representative 2D class averaged images of holo*Tv*FDPF3 particles. *B*, homology models docked into the reconstructed single-particle cryo-EM C2-symmetric map. *C*, distance between diiron center and FMN in the holo*Tv*FDPF3 FDP-like domain dimer. *D*, aligned overlay of the holo*Tv*FDPF3 FDP-like domain redox center with the redox center in ROO from *Desulfovibrio gigas* (Protein Data Bank ID: 1E5D) (18). *E*, aligned overlay of one holo*Tv*FDPF3 FDP-like domain subunit with a subunit of ROO from *D. gigas*, as aforementioned. *F*, surface representation of the dimerized FDP-like domain model with one subunit colored by hydrophobicity. A hydrophobic patch that is concealed in the *D. gigas* ROO head-to-tail dimer is highlighted. FDP, flavodiiron protein; *Tv*FDPF3, FDPF3 from *Trichomonas vaginalis*.

6.6 Å resolution map (Figs. S12, S13 and Table S5) with local resolutions ranging from 6.2 Å at the core of the particle to 7.0 Å at the periphery (Fig. S13*A*).

At this resolution, alpha helices could be clearly delineated, but a model could not be constructed *de novo*. We modeled individual domains by threading the *Tv*FDPF3 sequence onto structures of homologous proteins using PHYRE2 (43). The models were then manually docked into the cryo-EM density, revealing two FDP-like domains bound in a C2-symmetric dimer interface (Fig. S14). Electron density was noticeably poorer for one subunit of the dimer, potentially as a result of conformational heterogeneity produced by hinge motions at the dimer interface. We refined the density map again with C2 symmetry applied, resulting in a symmetric map with 6.8 Å nominal resolution, clear density for both subunits of the dimer, and local resolutions ranging from 5.4 Å to 6.9 Å (Figs. 6*B* and S15). Docking homology models of the FDP-like domain into the map with C2 symmetry applied produced a model equivalent to that generated from the original map without symmetry applied. In the final C2-symmetric map, density was observed for the diiron and FMN moieties in the positions expected from previously reported structures of FDPAs (Fig. S16).

The FDP-like domain of *Tv*FDPF3 forms an expected "head-to-tail" dimer that positions the diiron center of one protomer 8 to 10 Å away from the FMN moiety bound in the neighboring subunit (Fig. 6*C*). However, the dimer interface differs from that previously reported in structures of dimeric FDPAs from *Desulfovibrio gigas*, *Giardia intestinalis*, and *Moorella thermoacetica* (15, 18, 20). The *trans* interaction between the large subdomain of one subunit and the small subdomain of its neighbor is similar to structures reported previously (all-atom RMSD = 1.57 Å), with a 12° rotation about the redox center (Fig. 6*D*). The holo*Tv*FDPF3 dimer interface differs from that observed for FDPA from *D. gigas* (Rb:oxygen oxidoreductase) as a result of a 70° rotation about the linker connecting the large and small subdomains of the FDP-like core (Fig. 6*E*). This rotation substantially alters the interface between protomers (Fig. S17).

Discussion

There are substantial gaps in our understanding of core energy metabolism and redox maintenance in microaerophilic human parasites that belong to the *Excavata* supergroup (4, 44). Most of their proteomes, including key metabolic enzymes, are not well characterized and are annotated primarily based on sequence homology. In this work, we aimed to close this knowledge gap by biochemical and structural studies of the oxygen detoxification systems reported in *T. vaginalis* (4). The natural function of H_2O-forming NOXes and multicomponent FDPs in microaerophilic human protozoan parasites is both regeneration of oxidized pyridine dinucleotides and constant O_2 removal (detoxification) from the surroundings (Fig. 1*A*) (3, 4, 45, 46). In addition, these protozoa lack enzymes typically used to combat ROS, including catalase and superoxide dismutase, and are therefore dependent on the ability of the H_2O-forming oxidase reaction to remove O_2 before it can participate in the ROS-forming side reactions (3, 4, 46). Better understanding of the O_2 scavenging systems are needed as these pathways were recently suggested as targets for therapeutic interventions against various human protozoan parasites (3).

The presence of a NOX in *T. vaginalis*, and its general acceptance in the literature, was based on the original work of Linstead and Bradley from 1988 (3, 4, 9, 32). In this study, we show that in *T. vaginalis*, the closest homologs of a typical NOX enzyme are three very similar in amino acid sequence FDPFs that are currently misannotated in databases (TVAG_263800, TVAG_049830, and TVAG_121610) (Fig. 2*B* and Table S1). Based on domain organization, all three proteins harbor N-terminal FDP, central Rb, and C-terminal NROR domains (Fig. 2). Of note, Smutna *et al.* (29) previously suggested that TVAG_263800, TVAG_049830, and TVAG_121610 proteins are "self-sufficient" FDPs; however, this prediction was not tested, as only a "stand-alone" FDPA from *T. vaginalis* (TVAG_036010) was biochemically characterized at that time.

To directly test whether these genes encode "self-sufficient" FDPs, we overexpressed corresponding protein products in *E. coli* (Fig. S4, *A*–*F*). The initial kinetic characterization of these recombinant proteins revealed that despite variable and substoichiometric loading with FMN and iron, all three enzymes are capable of using NADH or NADPH as substrates (Tables 1, 2 and S2). The highest V_{max} (12 ± 1 μmol min^{-1} mg^{-1}) was observed for *Tv*FDPF3 with NADH. Notably, the FMN content is negatively correlated with the off-target H_2O_2 production as *Tv*FDPF1 (only 1% of FMN per monomer) mostly produces H_2O_2 (86 ± 5%) (Table S3). Once the FMN loading is ∼10% as in *Tv*FDPF3, the H_2O_2 production is significantly lower (9.6 ± 3.7%) and the NADH:O_2 stoichiometry is 2:1. Because the FMN cofactor is a part of the FeFe–FMN diiron active site, very low levels of FMN cofactor in *Tv*FDPF1 allow only a minor fraction of the four-electron H_2O-forming reaction to go until completion, and the most of reducing equivalents are used within the C-terminal NROR domain to produce exclusively H_2O_2. A similar phenomenon has been reported for NROR from *Clostridium acetobutylicum*, which is a H_2O_2-forming NOX. When *C. acetobutylicum* NROR is mixed with fprA2 (FDPA) and Rb, the NROR-Rb-fprA2 system starts to catalyze an efficient H_2O-forming oxidase reaction (22).

Next, we significantly optimized our purification scheme to obtain a highly active *Tv*FDPF3 with near-stoichiometric amounts of both FAD and FMN cofactors (holo*Tv*FDPF3) (Table 1 and Fig. 3, *A*–*D*). The iron content of holo*Tv*FDPF3 also improved to 1.70 ± 0.12 of Fe per monomer (Table S2). Most importantly, holo*Tv*FDPF3 had increased V_{max} of 291 ± 26 μmol min^{-1} mg^{-1} (k_{cat} = 466 ± 42 s^{-1} calculated per monomer) with K_m for NADH at 56 ± 2 μM (Table 2). We note that if an average of 1.3 Fe is missing from each dinuclear center, the turnover number under V_{max} conditions could be as high as 1310 s^{-1} or as high as 820 s^{-1}, if the missing 1.3 Fe is equally distributed over both dinuclear and the Rb sites ("all or

none"). The activity we are reporting of holo*Tv*FDPF3 is similar to that reported for FDPA from *E. histolytica* (400 ± 30 s^{-1}) (Table S6). In a recent study, FDPF from *C. difficile* was cloned and purified with iron and flavin content comparable to holo*Tv*FDPF3, and a 30-fold lower k_{cat} of 16.0 s^{-1} was reported (Table S6) (39).

Remarkably, the V_{max} we determined for holo*Tv*FDPF3 (466 ± 42 s^{-1}) agrees well with the V_{max} number reported for the native H_2O-forming NOX preparation from *T. vaginalis* from the study by Linstead and Bradley (470 s^{-1}) (32). In the original study, authors presented the purification of an H_2O-forming NOX activity that migrated as: (i) two close bands of ∼97 to 97.5 kDa on the SDS-PAGE and (ii) two very similar bands during isoelectric focusing (pIs ∼5.5) (32). This clearly represents a contradiction, as all known tDBDF family NOXes have molecular mass of ∼50 kDa. When we compared the pIs and molecular masses of *Tv*FDPF1–3, they matched exactly the behavior of protein samples described by Linstead and Bradley (32). For example, the pI of *Tv*FDPF1 (5.25) and pIs of *Tv*FDPF2–3 (5.75 and 5.63) can explain the two very close bands during isoelectric focusing. During late stages of our study, we learned that *Tv*FDPF2 was detected based on the mass spectrometric analysis in the cell lysate of *T. vaginalis*, and resulted protein was in-gel stained for the NOX activity (neither specific activity nor K_m was reported) (47). In the same study, a purification of recombinant *Tv*FDPF2 for the possible kinetic and spectroscopic analysis was not successful, and neither *Tv*FDPF1 nor *Tv*FDPF3 was detected in cell lysates (47).

Our work complements a recent study by Folgosa *et al.* (39) where authors determined redox potentials of redox cofactors that constitute the ET pathway within *C. difficile* FDPF. Here, we report a complete set of redox potentials that compose all four redox centers of the multidomain *Tv*FDPF3 (Fig. 5 and Table S7). The average redox potential, E_m= −235 mV (E_m = −241 [n = 1] and −229 mV [n = 1]) of the FAD within the NROR domain is very similar to potentials reported for *C. difficile* FDPF and "stand-alone" NRORs from *E. coli* and *Pyrococcus furiosus* (−237 ± 28 mV, Table S7). The redox potential of the $Fe(SCys)_4$ center (E_m = −56 mV, n = 1) is very similar to values reported in the literature for several "stand-alone" Rbs or the Rb-like domain of *C. difficile* FDPF (−67 ± 50 mV, Table S7). These values are very different from known redox potentials of the Rb-like center of nigrerythrin and rubrerythrin (+213 to +281 mV), which is surprising as the middle domain of FDPFs is maximally homologous to rubrerythrins. The redox potential of the FMN cofactor, −146 mV (n = 2) is similar to values reported for multiple FDPAs (−98 ± 66 mV; Table S7). Finally, in this study, we were able to determine the reduction potentials of the diiron center (E_m = −180 [n = 1] and +55 mV [n = 1]). We note that the redox potentials of the dinuclear iron center are more divergent, exemplified by *G. intestinalis* FDPA (E_m = +2 and +163 mV) (Table S7).

Our cryo-EM analysis revealed an unexpected architecture for the dimer interface of the N-terminal FDP core of holo*Tv*FDPF3. In contrast to previous structures of the head-to-tail "stand-alone" FDPAs (15, 18, 20), the subdomains of the FDP core exhibit a large rotation about the connecting linker, altering the dimerization interface while preserving the catalytic interface between the diiron center and FMN. We were unable to resolve electron density for Rb or NROR domains, suggesting that they may move flexibly relative to the central FDP-like core. This is not altogether unexpected, as the N-terminal FDP part is tethered to the other redox centers *via* an extended linker. It has been previously shown that FDPAs catalyze robust H_2O formation when Rb and NROR are supplied in *trans* (12, 19, 20, 35). The tethering of domains within *Tv*FDPF3 may increase the effective concentration of these domains and facilitate short-lived electron-shuttling intermediate conformations that were not well populated in our micrographs. Moreover, the larger-than-expected molecular masses observed in both size-exclusion chromatography and BN-PAGE for *Tv*FDPF1–3 suggest that the Rb-NROR domains contribute to an elongated protein shape (48). The reorganization of subdomains within the N-terminal FDP portion of *Tv*FDPF3 may hint at the interaction mechanism with the linked Rb and NROR domains. The subdomain rotation we observe in *Tv*FDPF3 exposes a hydrophobic surface that in structures of similar proteins is occluded within the dimerization interface (Fig. 6*F*). This surface is positioned approximately 35 Å away from the C-terminus of the nearest FDP-like small subdomain and approximately 10 Å away from the diiron/FMN reaction center. Although we did not observe electron density in this portion of the map, the long linker connecting the FDP-like and Rb domains could bridge this distance, permitting this surface to bind the Rb domain and complete ET with the NROR domain.

Both our structural insight and biochemical characterization bring up an important question about the ET pathway within the dimer of holo*Tv*FDPF3. Here, we propose that the most parsimonious flow of reducing equivalents is as follows: FAD → $Fe(SCys)_4$ → FMN within subunit 1 and then the diiron center of subunit 2 (Fig. 7). Spatial constraints make ET from the FAD to the $Fe(SCys)_4$ center of the other subunit very unlikely. The dimerization interface of holo*Tv*FDPF3 lies with the N-terminal FDP core, and therefore, it is unlikely that Rb and NROR from different protomers exchange electrons just like Fe–Fe and FMN centers do (Fig. 7). In summary, the two active sites within the dimer of "head-to-tail" FDP are formed, and electrons are relayed through Rb-NROR paths separately in both subunits 1 and 2 (Fig. 7). Testing our hypothesis of ET from NROR to the FMN and potential asymmetry in the ET pathway within active sites of the dimer of *Tv*FDPF3 is the next phase of our study.

Experimental procedures

Materials

All chemicals were purchased from Sigma–Aldrich, VWR, and Fisher Scientific unless otherwise specified. Menadiol (2-methyl-1,4-naphthalenediol) was from AK Scientific.

Bioinformatic analysis

The EuPathDB Bioinformatics Resource Center (https://eupathdb.org/eupathdb/) was used to browse genomic

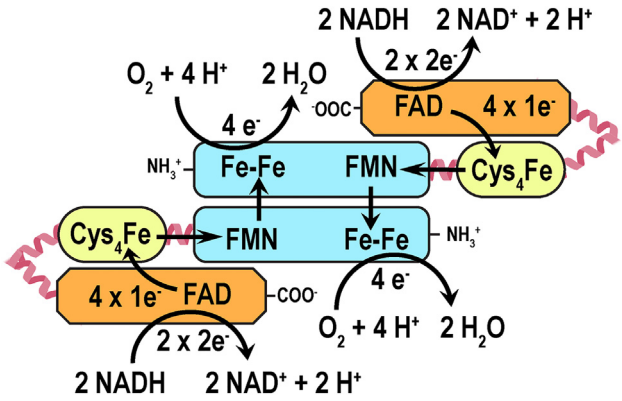

Figure 7. Proposed electron transport (ET) pathway within the dimer of holo*Tv*FDPF3. The FDP core domain with the Fe–Fe center and FMN is depicted in *light blue*, a Rb-like domain is depicted in *yellow*, and a NADH:Rb oxidoreductase (NROR) domain is depicted in *orange*. FDP, flavodiiron protein; Rb, rubredoxin; *Tv*FDPF3, FDPF3 from *Trichomonas vaginalis*.

sequences of *T. vaginalis* C3 and other eukaryotic microbes (49). Multiple sequence alignments were constructed using a stand-alone version of ClustalX 2.0 and edited using BOXSHADE 3.21.

Cloning of TvFDPF1–3 with a C-terminal hexa-histidine tag

Genomic DNA of *T. vaginalis* obtained from American Type Culture Collection (strain C-1:NIH [American Type Culture Collection 30001]) was used to PCR amplify the gene sequences encoding *Tv*FDPF1–3. The following primers were used to clone TVAG_263800 (*Tv*FDPF1) contained NdeI and XhoI restriction sites (underlined): forward 5'-TTA ATT CAT ATG CTT AAA ATT CAG CAA CTT ACA GAA GAT ATC-3′ and reverse 5'-TTA ATT CTC GAG AAA CAA TTC AGC AAG AAC GTG CTG TAA AGT ATG-3'. The following primers were used to clone TVAG_049830 (*Tv*FDPF2) contained NdeI and KpnI restriction sites (underlined): forward 5'-TTA ATT CAT ATG CTT AAA ATA CAG CAG CTC ACT GAA GAC-3′ and reverse 5'-TTA ATT GGT ACC TT GAA GAT TTC AGC CAT GAT GCG CTC TAA TG-3'. The following primers were used to clone TVAG_121610 (*Tv*FDPF3) contained AseI (creates an overhang compatible with the NdeI restriction site) and XhoI restriction sites (underlined): forward 5′-TTA ATT ATT AAT ATG CTT AAA ATT CAG CAG CTT ACA GAA GAT-3′ and reverse 5'-TTA ATT CTC GAG AAA TAC CTC AGC AAC AAC ACG CTG CAT TGA GTG-3'. All resulting PCR products were cloned into the pET30a expression vector (Novagen, EMD Millipore).

Initial expression and purification of TvFDPF1–3

All proteins in this study were overproduced in One Shot BL21 Star (DE3) chemically competent *E. coli* (Thermo Fisher [formerly Invitrogen]; catalog no.: C601003). Bacterial culture was grown at 37 °C in six 2.8 l flasks, each containing 1 l of Luria–Bertani medium (Becton, Dickinson and Company; catalog no.: 244610) supplemented with 50 μg/ml kanamycin until the absorbance at 600 nm reached 0.4 to 0.6. At that point, the temperature was decreased to 15 °C, and bacterial culture was grown for additional 2 h. After supplementation with 400 μM ammonium iron(II) sulfate hexahydrate and 0.1 mM isopropyl β-D-1-thiogalactopyranoside, bacterial cultures were grown overnight. For protein purification, *E. coli* cell pellet was resuspended in 120 ml of 50 mM sodium phosphate, pH 8.0, 500 mM NaCl, 30 mM imidazole (buffer A) containing 1 mg/ml of lysozyme, four cOmplete, EDTA-free, protease inhibitor cocktail tablets (Roche), 60 μl benzonase nuclease (EMD Millipore), and 4 mM PMSF and were disrupted by sonication on ice for 20 min at 30 s intervals separated by 60 s cooling periods. Following centrifugation, cell lysate was passed through a 0.4 μm syringe filter, diluted to ∼300 to 400 ml with buffer A, and loaded onto a 20 ml HisPrep FF 16/10 column (GE Healthcare/Cytiva). All chromatographic steps were performed using an AKTA Pure (GE Healthcare) or NGC Quest 10 Plus (Bio-Rad) chromatography systems. After washing HisPrep FF 16/10 column with 500 ml of buffer A, the gradient of 30 to 300 mM imidazole in buffer A was applied over 300 ml. Fractions containing *Tv*FDPF1–3 had distinct brown color and were exchanged into 50 mM sodium phosphate, pH 7.5 (buffer B). In the next step, protein sample in 40 ml of buffer B was applied onto a 30 ml Source 15Q column equilibrated with 50 mM sodium phosphate, pH 7.5, and 50 mM NaCl (buffer C) at a flow rate of 6 ml/min. Subsequently, Source 15Q column was washed with 150 ml of buffer C, and protein was eluted with 450 ml of gradient of 50 to 300 mM NaCl in buffer C. Size-exclusion chromatography was performed on a HiLoad 16/600 Superdex 200 (GE Healthcare/Cytiva; catalog no.: 28989335) or HiPrep 16/60 Sephacryl S-400 HR (GE Healthcare/Cytiva) columns equilibrated with 50 mM sodium phosphate, pH 7.5, 150 mM NaCl (buffer D) or with 50 mM Hepes–NaOH (pH 7.5), and 150 mM NaCl buffer (buffer E). Fractions containing protein of interest were pooled, concentrated, and flash-frozen in liquid nitrogen. Only affinity purification and size-exclusion chromatography steps were used for *Tv*FDPF2 because of its low stability and tendency to precipitate.

Determination of molecular weight by gel filtration

Analytical gel filtration was performed using a Superdex 200 Increase 10/300 GL column (GE Healthcare/Cytiva) operated at 0.9 ml/min in buffer E. Calibration curve was produced using thyroglobulin (669 kDa), ferritin (440 kDa), beta amylase from sweet potato (200 kDa), aldolase (158 kDa), conalbumin (75 kDa), bovine albumin (66 kDa), and ovalbumin (44 kDa). Molecular weight standards were from gel filtration kits (Sigma, catalog no.: MWGF200 and Cytiva, catalog no.: 28403842).

BN-PAGE

All BN-PAGE reagents were from Thermo Fisher Scientific. The anode buffer was prepared using 30 ml of 20× NativePAGE running buffer and 570 ml of milliQ water. Two hundred milliliters of "the light" and "the dark" cathode buffers was prepared using milliQ water, 10 ml of 2× NativePAGE running buffer, and

1 ml or 10 ml of cathode buffer additive. Protein samples were prepared using 4× NativePAGE sample buffer. Before the electrophoresis, wells of a 3 to 12% Novex Bis–Tris precast gel were filled with "the dark" cathode buffer. Samples and NativeMARK protein standards were added to assembled electrophoresis cell before "the dark" buffer was used to completely cover the inner chamber. Initial step of the electrophoresis was performed at 150 V until the dye front reached approximately one-third of the gel. Then "the dark" cathode buffer in the inner chamber was replaced with "the light" cathode buffer, and the run was continued till completion at 250 V. We also used recombinant H_2O-forming NOXes from *L. brevis* and *G. intestinalis* as additional molecular mass controls (12).

Purification of highly active holoTvFDPF3

The most active holo*Tv*FDPF3 enzyme was obtained using the protocol described previously but with several modifications. *E. coli* cells were grown in 6 l of Terrific broth medium, and for the homogenization step, cell pellet was resuspended in 400 ml of buffer A supplemented with 1 mg/ml of lysozyme, six cOmplete EDTA-free protease inhibitor cocktail tablets (Roche), 120 μl benzonase nuclease, and 4 mM PMSF. Affinity chromatography was performed using a self-packed 35 ml Ni Sepharose 6 Fast Flow column. For the anion-exchanger step, the Source 15Q column was equilibrated with 50 mM sodium phosphate, pH 7.5, and 15 mM NaCl (buffer F). The most active holo*Tv*FDPF3 (fully loaded with both FAD and FMN and superior specific activity in the 160–210 U/mg range) was eluting as a distinct peak during the 150 ml wash step with buffer F. We note that most of the protein was eluting in the gradient as described in the pevious section, but that protein fraction had very low specific activity compared with the highly active holo*Tv*FDPF3. Size-exclusion chromatography was performed in buffer E.

UV–visible spectroscopy

Cary 100 and Cary 3500 UV–visible spectrophotometers (Agilent) were used to record UV–visible spectra and perform activity assays under aerobic conditions. Anaerobic experiments were performed using Shimadzu 1900 UV–visible spectrometer installed inside a glove box (Coy Laboratory Products). Concentration of free FAD and FMN in solution was determined spectrophotometrically using extinction coefficients for FAD at 450 nm (11.3 mM^{-1} cm^{-1}) and for FMN at 446 nm (12.2 mM^{-1} cm^{-1}) (50).

Enzymatic assays

Enzyme activity was monitored by following the decrease of the absorbance of NADH or NADPH at 340 nm. A typical reaction mixture in 0.2 ml of buffer E was incubated for 3 min at 37 °C before NAD(P)H (0.5–600 μM) and enzyme (0.1–10 μg) were added. An extinction coefficient (ε_{340} = 6.2 mM^{-1} cm^{-1}) was used to calculate NAD(P)H oxidase activity. The k_{cat} values for *Tv*FDPF1–3 were calculated per monomer of the protein.

Near-simultaneous oxygen and NADH consumption were monitored using a custom-made instrument for measuring fluorescence spectra and time-resolved phosphorescence originally engineered for bioenergetics experiments with a suspension of purified mitochondria (the Mootha Laboratory, Massachusetts General Hospital). In the current set-up, NADH was monitored by its autofluorescence ($\lambda_{excitation}$ = 365 nm; $\lambda_{emision}$ = 440–460 nm), and oxygen was measured using the oxygen phosphorescence sensor spot SP-PSt6-NAU (PreSens Precision Sensing GmbH) affixed inside a quartz cuvette. Generally, enzyme (5–60 μg) and NAD(P)H (100–500 μM) were added to 0.5 ml of buffer E at 28 °C under regular oxygen tension. The instrument was operated using home-made software developed in LabView, Matlab, and Arduino Software IDE. Data from each experiment were exported as a text file and analyzed using SigmaPlot 13.0 (SYSTAT Software).

Determination of FAD and FMN content

Protein samples (10–50 μM of protein dimers as determined by the Bradford assay) or FAD/FMN standards (0–100 μM) in buffer E or ultrapure water were incubated at 95 °C for 10 min. After centrifugation at maximum speed, a 50-μl aliquot was added to 200 μl of 50%/50% methanol/acetonitrile solution, and the resulting samples were subjected to the LC–MS analysis. For the LC–MS analysis, running buffer G was 5% acetonitrile, 20 mM ammonium acetate, and 0.25% ammonium hydroxide, pH 9.0, whereas running buffer H was 100% acetonitrile. The gradient was run on a Dionex Ultimate 3000 system with an Xbridge amide column (2.1 × 100 mm, 2.5 μm particle size) at 220 μl/min flow rate, started at 85% H for 0.5 min, ramped to 35% H over the next 3.5 min, ramped to 2% H over the next 2 min, held at 2% H for 1 min, ramped to 85% H for 1.5 min, and then held at 85% H for 1.5 min (and ramping to 420 μl/min). The total run time was 12 min. The mass spectrometry analysis was performed on a Thermo QExactive Orbitrap mass spectrometer operated in polarity switching mode with a scan range of 70 to 1000 *m/z* and a resolving power of 70,000 at 200 *m/z*. The resulting data for FAD and FMN were processed using Xcalibur software (Thermo Fisher Scientific).

The FAD/FMN content was also analyzed on an Agilent 6495 QqQ with jet stream source coupled to an Agilent 1290 LC stack with an Agilent HILIC-Z (2.1 × 150 mm) column at the Scripps Center for Metabolomics (Department of Chemistry, The Scripps Research Institute). The mobile phase was composed of buffer I = 10 mM ammonium acetate, 5 μM medronic acid, pH = 9, buffer K = 90:10 acetonitrile/water, 10 mM ammonium acetate, 5 μM medronic acid, and pH = 9. The gradient started at 98% K (0–1 min) decreasing to 40% K (1–5 min) and was followed by an isocratic step (5–7 min) before a 5 min postrun for column re-equilibration. The flow rate was set to 250 μl/min, and the sample injection volume was 5 μl. Operating in negative-ion mode, the source conditions were as follows: drying gas temperature set to 200 °C with a flow rate of 11 l/min, the sheath gas temperature was 300 °C with a sheath gas flow rate of 12 l/min, the nebulizer pressure set to 35 psi, cap voltage set to 2500 V, and nozzle

voltage set to 1500 V. Data were processed using Agilent MassHunter Quantitative analysis software. All samples had values that were within the range of the calibration standards.

Iron determination with ferene

Proteins were diluted in buffer E to 10 to 40 μM of dimers. Iron standards were prepared using Mohr's Salt (ammonium iron(II) sulfate hexahydrate) in ultrapure water. Subsequently 100 μl of 1% hydrochloric acid were added to 100 μl aliquots of protein samples or iron standards, and tubes were incubated at 80 °C for 10 min. Next, 500 μl of 7.5% ammonium acetate were added with subsequent addition of 100 μl of 4% ascorbic acid, 100 μl of 2.5% sodium dodecyl sulphate, and 100 μl of iron chelator 3-(2-pyridyl)-5,6-bis(5-sulfo-2-furyl)-1,2,4-triazine disodium salt (samples were vortexed after each addition). After centrifugation at 13,000*g*, 800 μl of each sample were transferred to 1 ml plastic cuvettes to record absorbance at 592 nm.

Determination of H_2O_2 production

H_2O_2 production was monitored in a discontinuous assay. Large excess of the protein (5–30 μg) was added to the assay mixture that contained 110 μM NADH in 0.3 ml of buffer E and allowed to run at room temperature for 5 min (to establish full conversion of NADH to H_2O_2/H_2O). Aliquots of 50 μl were taken and added to another 50 μl of buffer E supplemented with 2 μl of horseradish peroxidase (Abcam; catalog no.: ab102500) and 2 μl Amplex Red (Abcam; catalog no.: ab102500). In parallel, a calibration curve with known amounts of H_2O_2 standards was constructed. Ten minutes later after incubating the assay mixture in a clear 96-well plate, the absorbance at 600 nm was recorded using EnVision 2103 plate reader (PerkinElmer).

Metal content determination by ICP-MS

The ICP-MS analysis was done on a Thermo Fisher Scientific iCAP RQ ICP-MS in the Environmental and Complex Analysis Laboratory (University of California, San Diego). Protein samples were prepared at 0.5 μM of monomers (10 ml) in 2% trace metal nitric acid and analyzed directly. The analysis was conducted in kinetic energy discrimination mode monitoring 45Sc and 89Y as internal standards.

EPR spectroscopy

The midpoint potentials of the Rb and dinuclear iron centers of holo*Tv*FDPF3 were determined from EPR signal intensities of the oxidized (as purified) and mixed-valence state, respectively. About 5 mg/ml holo*Tv*FDPF3 in (end volume 2 ml for the reductive titration with sodium dithionite and 1.5 ml for the oxidative titration with potassium ferricyanide) 50 mM Hepes–NaOH, pH 7.5, were stirred under anaerobic conditions at 298 K. The solution potential was measured with an InLab ARGENTHAL microelectrode (Ag/AgCl, +207 mV *versus* H_2/H^+ with in-built Pt counter electrode) in the presence of phenazine ethosulfate, methylene blue, resorufin, indigo carmine, 2-hydroxy-1,4-naphthoquinone, *N*,*N*,*N*,*N*-tetramethyl-*p*-phenylendiamine, sodium anthraquinone-2-sulfonate, phenosafranin, safranin T, neutral red, benzylviologen, and methylviologen (all at final concentration of 20 μM). After adjustment of the potential by microliter additions of the sodium dithionite or potassium ferricyanide and 5 min equilibration, samples were withdrawn, removed from the anaerobic glove box in EPR tubes closed with inner diameter 3 mm × outer diameter (OD) 7 mm natural rubber tubing with 5 mm OD acrylic glass round stick. Samples were stored in liquid nitrogen until EPR spectra were recorded. For the menadiol-treated sample, 300 μl of 7 mg/ml holo*Tv*FDP3 with the first five mediators (at 10 μM) were titrated to a potential of +115 mV *versus* H_2/H^+ with sodium dithionite. Thereafter, menadiol was added to a final concentration of 50 μM. EPR spectra were recorded with a digitally upgraded Bruker Elexsys E580 X band spectrometer with a 4122HQE cavity, an Oxford Instruments ESR 900 helium flow cryostat, and the cryocooling system composed of a Stinger (Cold Edge Technologies) closed-cycle cryostat linked to an F-70 Sumitomo helium compressor. EPR tubes were produced by a local glassblower from Ilmasil PN tubing with OD 4.7 mm and 0.5 mm wall thickness obtained from Qsil.

UV–visible NAD^+ and redox titrations

*Tv*FDPF3 (6.4 μM) or *Tv*FDPF3 with a low FMN content (7.9 μM FAD) in buffer E was completely reduced by addition of sodium dithionite (1 mM final concentration). Increments of a 1 to 2 μM NAD^+ in the same buffer were added. For the NAD^+ titration experiment, the sodium dithionite powder was transferred into the anaerobic tent and dissolved in anaerobic buffer E. It was left to stand for 30 min: traces of oxygen, if any, would be reduced. *Tv*FDPF3 was incubated in the tent with careful occasional pipetting to have the O_2 of the small-volume aerobic stock solution diffuse out for 30 min. Then it was diluted into anaerobic buffer E, which had been bubbled with tent atmosphere for 3 h. For the titration, NAD^+ powder was dissolved in an anaerobic buffer and shaken vigorously in the tent to remove traces of O_2 in the NAD^+. The NAD^+ solution was standardized by measurement of the absorbance at 260 nm (ε260 = 17.8 mM^{-1} cm^{-1}). Since the absorbance increase at 704 nm upon binding of NAD^+ to $FADH_2$ was moderate (≈0.02), we corrected for minor baseline shifts by subtracting the absorbance at 900 nm. To better represent the region at which NAD^+ is nearly stoichiometric to $FADH_2$, we used an estimated of $K_D \approx 0.13$ μM for the fit, both for *Tv*FDPF3 with high and low FMN content. The experimental error for the stoichiometry was calculated from doubling of the least squares between experiment and fit.

The UV–visible redox titration using a mixture of methylene blue, resorufin, indigo carmine, 2-hydroxy-1,4-naphthoquinone, sodium anthraquinone-2-sulfonate, phenosafranin, safranin T, neutral red (all at a final concentration of 5 μM) was performed by monitoring the absorbance at 425 nm (minus the absorbance at 900 nm) using a Shimadzu 1900 UV–visible spectrometer installed inside the Coy glove box. At this wavelength, minimal changes for the mediator mix without *Tv*FDPF3 occurred, whereas the bleaching of the flavin absorbance upon reduction is substantial. For subtraction of the mediator contribution at

potentials which did not exactly match that of the *Tv*FDPF3 titrations, a polynomial best representing the dependence of the absorbance at 425 nm for mediator-only titrations was used. The net observed absorbance at 425 nm as function of solution potential was then fitted to the sum of the contributions for two flavins and a small contribution for the Rb center at high potential, all calculated from the Nernst equation. The absorbance at 600 minus 650 nm was used for the titration of the neutral semiquinone. For the semiquinone content per FAD of deFMN-*Tv*FDPF3, an extinction coefficient at 600 nm of 2.8 mM^{-1} cm^{-1} was used, derived from Figure 2 in Ref. (41). The data on holo*Tv*FDPF3 were less accurate, but the relative semiquinone absorbance features per FAD were similar. From the Nernst equation for two consecutive (n = 1) redox transitions, the maximum fractional population of the semiquinone intermediate was calculated. The neutral semiquinone content per FAD was then used to estimate the separation of the two redox potentials (Figs. 5*E* and S11, *B* and *C*).

Half reaction of TvFDPF3 in the presence of NONOate

A stock solution (10 mM) of diethylamine NONOate sodium salt hydrate (Sigma–Aldrich) was prepared by dissolving 3.9 mg in 245 μl of deoxygenated 10 mM KOH (prepared by bubbling nitrogen in the anaerobic tent). Transfer of electrons from NADH to NO in the reaction catalyzed by *Tv*FDPF3 was monitored at 340 nm using a Shimadzu UV-310 spectrophotometer in the Coy tent. To release NO the assay buffer, NADH (200 μM) and NONOate (100 μM) were mixed and incubated for 5 min. Next, 120 μg of the enzyme were added, and absorbance or spectral changes were followed as a function of time. Samples where enzyme or NONOate were omitted served as controls.

Cryo-EM sample preparation and data collection

Purified highly active holo*Tv*FDPF3 was diluted to 0.8 mg/ml using buffer E, and 4 μl was applied to a glow-discharged Quantifoil 200 mesh 1.2/1.3 Cu holey carbon grid (Electron Microscopy Sciences). Excess sample was removed by blotting with a Vitrobot Mark IV (Thermo Fisher Scientific) for 5 s at +15 blotting force in an environment held at 22 °C and 100% relative humidity, then the grid was frozen by plunging into liquid ethane. The frozen grid was imaged at 300 kV with a Titan Krios microscope (Thermo Fisher Scientific) with a slit energy filter (Gatan) set to 20 eV. Images were acquired in counting mode (105,000× nominal magnification, 0.825 Å pixel size) on a K3 direct electron detector (Gatan). Acquisitions were stored as 51-frame dose-weighted movies with defocus ranging from −1.3 to −2.5 μm. Each movie was collected with a 1.8 s total exposure time, a 30.3 e^{-} $Å^{-2}$ $frame^{-1}$ specific dose, and a 54.5 e^{-} $Å^{-2}$ overall electron dose. SerialEM 3.8.6 was used to automate multishot image acquisition, and 7398 total movies were collected (51).

Cryo-EM data processing

The holo*Tv*FDPF3 image dataset was processed using CryoSPARC 3.2.0 to pick an initial particle set and RELION 3.1.3 to curate particles and refine maps (Fig. S12) (52, 53). All micrographs were imported into CryoSPARC and preprocessed using the CryoSPARC internal patch motion correction and patch contrast transfer function (CTF) estimation jobs. An initial particle set was generated by blob picking particles between 80 Å and 180 Å in diameter from all micrographs. These particles were twice sequentially subjected to 2D classification, and the best classes were selected. The micrographs were then manually curated to remove images with minimum CTF fits of 9 Å or greater. After curation, 6938 of the original 7398 movies remained under consideration. The 2D classes selected from blob picking were used to train a Topaz model, and the model was used to pick particles from the curated micrographs (54). Duplicate particles were removed by excluding particles with a center within 125 Å of another particle. The coordinates of the remaining 1,511,632 particles were then encoded into star files for import into RELION using a custom python script, made available at https://github.com/tribell4310/reliosparc. The original set of 7398 movies was separately imported into RELION and preprocessed using RELION's implementations of MotionCor2 1.2.6 and CTFFIND 4.1.13 (55, 56). STAR files containing the coordinates of particles selected in cryoSPARC were then imported into RELION and used to extract particles from the RELION-preprocessed movies with a 256 pixel box size and no binning. The particle stack was subjected to three sequential rounds of 2D classification, with the best classes selected in each iteration. The particles were recentered by 3D autorefinement using an initial model generated *de novo* in RELION from a larger set of curated particles. The recentered particles were then re-extracted from micrographs with a 256 pixel box size and no binning using the refined particle coordinates. These particles were subjected to an additional cycle of 2D classification to remove any particles that would not align well after recentering. The best classes were then 3D autorefined, and the resulting volume was used to create a mask with a 9 pixel extension and a 7 pixel soft edge. The mask was then applied during 3D classification of the particle set into six classes using a *tau_fudge* parameter of 20, as has previously been used to resolve structural features in small targets (57). Two density types emerged from 3D classification: a compact map with well-resolved features and a low-resolution extended map with poor density, which may correspond to a more flexible conformation of the protein. Subsequent masked 3D classification of the compact classes did not improve the quality of the map, so all 101,628 particles in the compact conformation were included in the final particle stack. The compact conformation particles were autorefined twice with progressively tighter masks, first with a mask with a 9 pixel extension and a 7 pixel soft edge, and then with a 7 pixel extension and a 7 pixel soft edge. The last masked refinement was then subjected to three sequential rounds of RELION's CTF refinement protocol, producing a map with 7.0 Å overall resolution. Finally, the map was sharpened by applying a *B*-factor of −534.7, estimated during the RELION postprocessing protocol. The final sharpened map had an overall resolution of 6.6 Å. After modeling indicated likely C2 symmetry in the

map, the set of 130,196 particles from 2D classes represented in the C1 map was three-dimensionally classified with C2 symmetry applied, a 150 Å diameter spherical mask, a *tau_fudge* factor of 20, and the C1 refined map lowpass filtered to 50 Å as an input template. Two similar compact classes emerged and were subjected to a subsequent round of unmasked 3D classification. A homogeneous class containing 53,709 particles was identified and 3D autorefined with a mask (6 pixel extension, 4 pixel soft edge), then CTF refined using the same protocol as aforementioned, resulting in a 6.6 Å unsharpened map. The map was sharpened with a *B*-factor of −658.7 using the RELION postprocessing protocol, producing a final map with 6.8 Å nominal resolution. Local resolutions were estimated using RELION's integrated local resolution estimation algorithm (58).

Model building

Because the resolution of the final maps was insufficient to build atomic models *de novo*, the model was constructed using homology models from individual domains. Homology models were generated using the PHYRE2 server, and with 92% of the *Tv*FDPF3 sequence covered between three models (43). Residues 2 to 366 (N-terminal FDP-like domain) were modeled onto the Protein Data Bank (PDB) 1VME structure (FDPA from *Thermotoga maritima*), residues 428 to 472 (Rb domain) were modeled onto the PDB 1LKO structure (rubrerythrin from *Desulfovibrio vulgaris*), and residues 482 to 871 (the C-terminal NROR domain) were modeled onto the PDB 3NTA structure (NADH-dependent persulfide reductase from *Shewanella loihica*). Appropriate ligands were included in the homology models based on their conserved binding pockets in homologous structures. The map was consistent with a dimer of FDP-like domains, and models were built by manually placing homology models in density using UCSF Chimera (59), with the N- and C-terminal subdomains of the FDP-like domain separated to facilitate the large rotation between the subdomains. Once the subdomains were confidently placed, we verified that the domain placements were topologically reasonable by modeling the connecting linker region using the next-generation kinematic closure loop modeling protocol in Rosetta (60). The model was refined to the C2-symmetric map using a single application of real-space refinement in Phenix (61). Structural alignments comparing *Tv*FDPF3 with the head-to-tail dimer form of Rb:oxygen oxidoreductase from *D. gigas* (PDB ID: 1E5D) were performed using PyMol (62). Figures were generated using UCSF Chimera and PyMol (59, 62).

Data availability

The cryo-EM maps of holo*Tv*FDPF3 have been deposited into the Electron Microscopy Data Bank (EMDB; accession nos.: EMD-25790 and EMD-25787), and the underlying particle images have been deposited with the Electron Microscopy Public Image Archive (EMPIAR) (accession no.: EMPIAR-10895). The docked homology models have been deposited in Zenodo (https://doi.org/10.5281/zenodo.5795907). All the other data are contained within this article.

Supporting information—This article contains supporting information (63–73).

Acknowledgments—Cryo-EM data were collected at the Harvard Cryo-EM Center for Structural Biology at Harvard Medical School. We thank Xue Fei (Massachusetts Institute of Technology) and Michelle Fry (Massachusetts General Hospital) for helpful feedback during cryo-EM map refinement. We thank the anonymous reviewers for very constructive suggestions.

Author contributions—V. K. M. and V. C. conceptualization; E. N. A., T. A. B., B. R., M. L. H., T. B., O. S. S., M. A. Y., L. H. C., A. J. P., and V. C. investigation; L. H. C., V. K. M., A. J. P., and V. C. resources; E. N. A., T. A. B., L. H. C., A. J. P., and V. C. writing-original draft; E. N. A., T. A. B., B. R., M. L. H., T. B., O. S. S., M. A. Y., L. H. C., V. K. M., A. J. P., and V. C. writing-review and editing; V. K. M. and V. C. supervision.

Funding and additional information—This work was supported by grants from the National Institutes of Health (grant nos.: R00GM121856 and R35GM142495 [to V. C.], R35GM142553 [to L. H. C.], F32GM133047 [to O. S. S.], R35GM122455, and T-R01GM099683 [to V. K. M.], R00AG042026, and R01AA027097 [to M. A. Y.]) and from the Helen Hay Whitney Foundation (to T. A. B). V. K. M. is an Investigator of the Howard Hughes Medical Institute. A. J. P. acknowledges the DFG (project number 444947649, INST 248/320-1 FUGG) and the government of Rhineland-Palatinate for the upgrade of the EPR spectrometer. The content is solely the responsibility of the authors and does not necessarily represent the official views of the National Institutes of Health.

Conflict of interest—V. K. M. and V. C. are listed as inventors on a patent application filed by Massachusetts General Hospital on the therapeutic uses of water-forming NOXs. V. K. M. is a scientific advisor to and receives equity from 5AM Ventures and Janssen Pharmaceuticals. O. S. S. was a paid consultant for Proteinaceous, Inc. All other authors declare that they have no conflicts of interest with the contents of this article.

Abbreviations—The abbreviations used are: BN-PAGE, blue native-PAGE; CTF, contrast transfer function; EPR, electron paramagnetic resonance; ET, electron transfer; ETC, electron transport chain; FDP, flavodiiron protein; FDPA, class A FDP; FDPF, class F FDP; ICP-MS, inductively coupled plasma mass spectrometry; NO, nitric oxide; NOX, H_2O-forming NADH oxidase; NROR, NAD(P)H:rubredoxin oxidoreductase; OD, outer diameter; PDB, Protein Data Bank; Rb, rubredoxin; ROS, reactive oxygen species; tDBDF, two dinucleotide-binding domain flavoprotein; TvFDPF, class F FDP from *Trichomonas vaginalis*.

References

1. Hodges, A. L., and Holland, A. C. (2018) Common sexually transmitted infections in women. *Nurs. Clin. North Am.* **53**, 189–202
2. Mark, H., Dhir, A., and Roth, C. (2015) CE: sexually transmitted infections in the United States: overview and update. *Am. J. Nurs.* **115**, 34–44
3. Leitsch, D., Williams, C. F., and Hrdy, I. (2018) Redox pathways as drug targets in microaerophilic parasites. *Trends Parasitol.* **34**, 576–589

4. Muller, M., Mentel, M., van Hellemond, J. J., Henze, K., Woehle, C., Gould, S. B., *et al.* (2012) Biochemistry and evolution of anaerobic energy metabolism in eukaryotes. *Microbiol. Mol. Biol. Rev.* **76**, 444–495
5. Baernstein, H. D. (1963) A review of electron transport mechanisms in parasitic protozoa. *J. Parasitol.* **49**, 12–21
6. Brown, D. M., Upcroft, J. A., Edwards, M. R., and Upcroft, P. (1998) Anaerobic bacterial metabolism in the ancient eukaryote Giardia duodenalis. *Int. J. Parasitol.* **28**, 149–164
7. Wallen, J. R., Mallett, T. C., Okuno, T., Parsonage, D., Sakai, H., Tsukihara, T., *et al.* (2015) Structural analysis of Streptococcus pyogenes NADH oxidase: conformational dynamics involved in formation of the C(4a)-peroxyflavin intermediate. *Biochemistry* **54**, 6815–6829
8. Ross, R. P., and Claiborne, A. (1992) Molecular cloning and analysis of the gene encoding the NADH oxidase from Streptococcus faecalis 10C1. Comparison with NADH peroxidase and the flavoprotein disulfide reductases. *J. Mol. Biol.* **227**, 658–671
9. Ojha, S., Meng, E. C., and Babbitt, P. C. (2007) Evolution of function in the "two dinucleotide binding domains" flavoproteins. *PLoS Comput. Biol.* **3**, e121
10. Ogboo, B. C., Grabovyy, U. V., Maini, A., Scouten, S., van der Vliet, A., Mattevi, A., *et al.* (2022) Architecture of the NADPH oxidase family of enzymes. *Redox Biol.* **52**, 102298
11. Lountos, G. T., Jiang, R., Wellborn, W. B., Thaler, T. L., Bommarius, A. S., and Orville, A. M. (2006) The crystal structure of NAD(P)H oxidase from lactobacillus sanfranciscensis: insights into the conversion of O2 into two water molecules by the flavoenzyme. *Biochemistry* **45**, 9648–9659
12. Titov, D. V., Cracan, V., Goodman, R. P., Peng, J., Grabarek, Z., and Mootha, V. K. (2016) Complementation of mitochondrial electron transport chain by manipulation of the NAD+/NADH ratio. *Science* **352**, 231–235
13. Goncalves, V. L., Vicente, J. B., Pinto, L., Romao, C. V., Frazao, C., Sarti, P., *et al.* (2014) Flavodiiron oxygen reductase from Entamoeba histolytica: modulation of substrate preference by tyrosine 271 and lysine 53. *J. Biol. Chem.* **289**, 28260–28270
14. Silaghi-Dumitrescu, R., Coulter, E. D., Das, A., Ljungdahl, L. G., Jameson, G. N., Huynh, B. H., *et al.* (2003) A flavodiiron protein and high molecular weight rubredoxin from Moorella thermoacetica with nitric oxide reductase activity. *Biochemistry* **42**, 2806–2815
15. Silaghi-Dumitrescu, R., Kurtz, D. M., Jr, Ljungdahl, L. G., and Lanzilotta, W. N. (2005) X-ray crystal structures of Moorella thermoacetica FprA. Novel diiron site structure and mechanistic insights into a scavenging nitric oxide reductase. *Biochemistry* **44**, 6492–6501
16. Vicente, J. B., Carrondo, M. A., Teixeira, M., and Frazao, C. (2008) Structural studies on flavodiiron proteins. *Met. Enzymol.* **437**, 3–19
17. Vicente, J. B., Justino, M. C., Goncalves, V. L., Saraiva, L. M., and Teixeira, M. (2008) Biochemical, spectroscopic, and thermodynamic properties of flavodiiron proteins. *Met. Enzymol.* **437**, 21–45
18. Frazao, C., Silva, G., Gomes, C. M., Matias, P., Coelho, R., Sieker, L., *et al.* (2000) Structure of a dioxygen reduction enzyme from Desulfovibrio gigas. *Nat. Struct. Biol.* **7**, 1041–1045
19. Page, C. C., Moser, C. C., Chen, X., and Dutton, P. L. (1999) Natural engineering principles of electron tunnelling in biological oxidation-reduction. *Nature* **402**, 47–52
20. Di Matteo, A., Scandurra, F. M., Testa, F., Forte, E., Sarti, P., Brunori, M., *et al.* (2008) The O2-scavenging flavodiiron protein in the human parasite Giardia intestinalis. *J. Biol. Chem.* **283**, 4061–4068
21. Jenney, F. E., Jr., and Adams, M. W. (2001) Rubredoxin from pyrococcus furiosus. *Met. Enzymol.* **334**, 45–55
22. Kawasaki, S., Sakai, Y., Takahashi, T., Suzuki, I., and Niimura, Y. (2009) O2 and reactive oxygen species detoxification complex, composed of O2-responsive NADH:rubredoxin oxidoreductase-flavoprotein A2-desulfoferrodoxin operon enzymes, rubperoxin, and rubredoxin, in Clostridium acetobutylicum. *Appl. Environ. Microbiol.* **75**, 1021–1029
23. Lee, W. Y., Brune, D. C., LoBrutto, R., and Blankenship, R. E. (1995) Isolation, characterization, and primary structure of rubredoxin from the photosynthetic bacterium, Heliobacillus mobilis. *Arch. Biochem. Biophys.* **318**, 80–88
24. LeGall, J., Prickril, B. C., Moura, I., Xavier, A. V., Moura, J. J., and Huynh, B. H. (1988) Isolation and characterization of rubrerythrin, a non-heme iron protein from Desulfovibrio vulgaris that contains rubredoxin centers and a hemerythrin-like binuclear iron cluster. *Biochemistry* **27**, 1636–1642
25. Lovenberg, W., and Sobel, B. E. (1965) Rubredoxin: a new electron transfer protein from Clostridium pasteurianum. *Proc. Natl. Acad. Sci. U. S. A.* **54**, 193–199
26. Folgosa, F., Martins, M. C., and Teixeira, M. (2018) Diversity and complexity of flavodiiron NO/O2 reductases. *FEMS Microbiol. Lett.* **365**. https://doi.org/10.1093/femsle/fnx267
27. Romao, C. V., Vicente, J. B., Borges, P. T., Frazao, C., and Teixeira, M. (2016) The dual function of flavodiiron proteins: oxygen and/or nitric oxide reductases. *J. Biol. Inorg. Chem.* **21**, 39–52
28. Saraiva, L. M., Vicente, J. B., and Teixeira, M. (2004) The role of the flavodiiron proteins in microbial nitric oxide detoxification. *Adv. Microb. Physiol.* **49**, 77–129
29. Smutna, T., Goncalves, V. L., Saraiva, L. M., Tachezy, J., Teixeira, M., and Hrdy, I. (2009) Flavodiiron protein from Trichomonas vaginalis hydrogenosomes: the terminal oxygen reductase. *Eukaryot. Cell* **8**, 47–55
30. Vicente, J. B., Tran, V., Pinto, L., Teixeira, M., and Singh, U. (2012) A detoxifying oxygen reductase in the anaerobic protozoan Entamoeba histolytica. *Eukaryot. Cell* **11**, 1112–1118
31. Tanabe, M. (1979) Trichomonas vaginalis: NADH oxidase activity. *Exp. Parasitol.* **48**, 135–143
32. Linstead, D. J., and Bradley, S. (1988) The purification and properties of two soluble reduced nicotinamide: acceptor oxidoreductases from Trichomonas vaginalis. *Mol. Biochem. Parasitol.* **27**, 125–133
33. Brown, D. M., Upcroft, J. A., and Upcroft, P. (1996) A H2O-producing NADH oxidase from the protozoan parasite Giardia duodenalis. *Eur. J. Biochem. FEBS* **241**, 155–161
34. Castillo-Villanueva, A., Mendez, S. T., Torres-Arroyo, A., Reyes-Vivas, H., and Oria-Hernandez, J. (2016) Cloning, expression and characterization of recombinant, NADH oxidase from Giardia lamblia. *Protein J.* **35**, 24–33
35. Vicente, J. B., Testa, F., Mastronicola, D., Forte, E., Sarti, P., Teixeira, M., *et al.* (2009) Redox properties of the oxygen-detoxifying flavodiiron protein from the human parasite Giardia intestinalis. *Arch. Biochem. Biophys.* **488**, 9–13
36. Nishikawa, K., Shomura, Y., Kawasaki, S., Niimura, Y., and Higuchi, Y. (2010) Crystal structure of NADH:rubredoxin oxidoreductase from Clostridium acetobutylicum: a key component of the dioxygen scavenging system in obligatory anaerobes. *Proteins* **78**, 1066–1070
37. Hagelueken, G., Wiehlmann, L., Adams, T. M., Kolmar, H., Heinz, D. W., Tummler, B., *et al.* (2007) Crystal structure of the electron transfer complex rubredoxin rubredoxin reductase of Pseudomonas aeruginosa. *Proc. Natl. Acad. Sci. U. S. A.* **104**, 12276–12281
38. Ahmed, S. A., and Claiborne, A. (1989) The streptococcal flavoprotein NADH oxidase. II. Interactions of pyridine nucleotides with reduced and oxidized enzyme forms. *J. Biol. Chem.* **264**, 19863–19870
39. Folgosa, F., Martins, M. C., and Teixeira, M. (2018) The multidomain flavodiiron protein from Clostridium difficile 630 is an NADH:oxygen oxidoreductase. *Sci. Rep.* **8**, 10164
40. Massey, V., and Palmer, G. (1966) On the existence of spectrally distinct classes of flavoprotein semiquinones. A new method for the quantitative production of flavoprotein semiquinones. *Biochemistry* **5**, 3181–3189
41. Valentino, H., Korasick, D. A., Bohac, T. J., Shapiro, J. A., Wencewicz, T. A., Tanner, J. J., *et al.* (2021) Structural and biochemical characterization of the flavin-dependent siderophore-interacting protein from Acinetobacter baumannii. *ACS Omega* **6**, 18537–18547
42. Zanetti, G., Williams, C. H., Jr, and Massey, V. (1968) Influence of photoirradiation on the oxidation-reduction state of thioredoxin reductase. *J. Biol. Chem.* **243**, 4013–4019
43. Kelley, L. A., Mezulis, S., Yates, C. M., Wass, M. N., and Sternberg, M. J. (2015) The Phyre2 web portal for protein modeling, prediction and analysis. *Nat. Protoc.* **10**, 845–858
44. Hampl, V., Hug, L., Leigh, J. W., Dacks, J. B., Lang, B. F., Simpson, A. G., *et al.* (2009) Phylogenomic analyses support the monophyly of Excavata and resolve relationships among eukaryotic "supergroups". *Proc. Natl. Acad. Sci. U. S. A.* **106**, 3859–3864

45. Gao, H., Li, J., Sivakumar, D., Kim, T. S., Patel, S. K. S., Kalia, V. C., *et al.* (2019) NADH oxidase from lactobacillus reuteri: a versatile enzyme for oxidized cofactor regeneration. *Int. J. Biol. Macromol.* **123**, 629–636
46. Higuchi, M. (1992) Reduced nicotinamide adenine dinucleotide oxidase involvement in defense against oxygen toxicity of Streptococcus mutans. *Oral Microbiol. Immunol.* **7**, 309–314
47. Lamien-Meda, A., and Leitsch, D. (2020) Identification of the NADH-oxidase gene in Trichomonas vaginalis. *Parasitol. Res.* **119**, 683–686
48. Erickson, H. P. (2009) Size and shape of protein molecules at the Nanometer level determined by sedimentation, gel filtration, and electron microscopy. *Biol. Procedures Online* **11**, 32
49. Warrenfeltz, S., Basenko, E. Y., Crouch, K., Harb, O. S., Kissinger, J. C., Roos, D. S., *et al.* (2018) EuPathDB: the eukaryotic pathogen genomics database Resource. *Met. Mol. Biol.* **1757**, 69–113
50. Aliverti, A., Curti, B., and Vanoni, M. A. (1999) Identifying and quantitating FAD and FMN in simple and in iron-sulfur-containing flavoproteins. *Met. Mol. Biol.* **131**, 9–23
51. Mastronarde, D. N. (2005) Automated electron microscope tomography using robust prediction of specimen movements. *J. Struct. Biol.* **152**, 36–51
52. Punjani, A., Rubinstein, J. L., Fleet, D. J., and Brubaker, M. A. (2017) cryoSPARC: algorithms for rapid unsupervised cryo-EM structure determination. *Nat. Met.* **14**, 290–296
53. Zivanov, J., Nakane, T., Forsberg, B. O., Kimanius, D., Hagen, W. J., Lindahl, E., *et al.* (2018) New tools for automated high-resolution cryo-EM structure determination in RELION-3. *Elife* **7**, e42166
54. Bepler, T., Morin, A., Rapp, M., Brasch, J., Shapiro, L., Noble, A. J., *et al.* (2019) Positive-unlabeled convolutional neural networks for particle picking in cryo-electron micrographs. *Nat. Met.* **16**, 1153–1160
55. Zheng, S. Q., Palovcak, E., Armache, J. P., Verba, K. A., Cheng, Y., and Agard, D. A. (2017) MotionCor2: anisotropic correction of beam-induced motion for improved cryo-electron microscopy. *Nat. Met.* **14**, 331–332
56. Rohou, A., and Grigorieff, N. (2015) CTFFIND4: fast and accurate defocus estimation from electron micrographs. *J. Struct. Biol.* **192**, 216–221
57. Herzik, M. A., Jr., Wu, M., and Lander, G. C. (2019) High-resolution structure determination of sub-100 kDa complexes using conventional cryo-EM. *Nat. Commun.* **10**, 1032
58. Kucukelbir, A., Sigworth, F. J., and Tagare, H. D. (2014) Quantifying the local resolution of cryo-EM density maps. *Nat. Met.* **11**, 63–65
59. Pettersen, E. F., Goddard, T. D., Huang, C. C., Couch, G. S., Greenblatt, D. M., Meng, E. C., *et al.* (2004) UCSF Chimera–a visualization system for exploratory research and analysis. *J. Comput. Chem.* **25**, 1605–1612
60. Stein, A., and Kortemme, T. (2013) Improvements to robotics-inspired conformational sampling in rosetta. *PLoS One* **8**, e63090
61. Afonine, P. V., Poon, B. K., Read, R. J., Sobolev, O. V., Terwilliger, T. C., Urzhumtsev, A., *et al.* (2018) Real-space refinement in PHENIX for cryo-EM and crystallography. *Acta Crystallogr. D Struct. Biol.* **74**, 531–544
62. *The PyMOL Molecular Graphics System, Version 2.0.* (2015). Schrödinger, LLC, New York, NY
63. Hayashi, T., Caranto, J. D., Wampler, D. A., Kurtz, D. M., and Moenne-Loccoz, P. (2010) Insights into the nitric oxide reductase mechanism of flavodiiron proteins from a flavin-free enzyme. *Biochemistry* **49**, 7040–7049
64. Silaghi-Dumitrescu, R., Ng, K. Y., Viswanathan, R., and Kurtz, D. M., Jr. (2005) A flavo-diiron protein from Desulfovibrio vulgaris with oxidase and nitric oxide reductase activities. Evidence for an in vivo nitric oxide scavenging function. *Biochemistry* **44**, 3572–3579
65. Hillmann, F., Riebe, O., Fischer, R. J., Mot, A., Caranto, J. D., Kurtz, D. M., Jr., *et al.* (2009) Reductive dioxygen scavenging by flavo-diiron proteins of Clostridium acetobutylicum. *FEBS Lett.* **583**, 241–245
66. Saeki, K., Jain, M. K., Shen, G. J., Prince, R. C., and Zeikus, J. G. (1989) Purification and properties of ferredoxin and rubredoxin from Butyribacterium methylotrophicum. *J. Bacteriol.* **171**, 4736–4741
67. Yoon, K. S., Hille, R., Hemann, C., and Tabita, F. R. (1999) Rubredoxin from the green sulfur bacterium Chlorobium tepidum functions as an electron acceptor for pyruvate ferredoxin oxidoreductase. *J. Biol. Chem.* **274**, 29772–29778
68. Swartz, P. D., Beck, B. W., and Ichiye, T. (1996) Structural origins of redox potentials in Fe-S proteins: electrostatic potentials of crystal structures. *Biophys. J.* **71**, 2958–2969
69. Vicente, J. B., and Teixeira, M. (2005) Redox and spectroscopic properties of the Escherichia coli nitric oxide-detoxifying system involving flavorubredoxin and its NADH-oxidizing redox partner. *J. Biol. Chem.* **280**, 34599–34608
70. Pierik, A. J., Wolbert, R. B., Portier, G. L., Verhagen, M. F., and Hagen, W. R. (1993) Nigerythrin and rubrerythrin from Desulfovibrio vulgaris each contain two mononuclear iron centers and two dinuclear iron clusters. *Eur. J. Biochem.* **212**, 237–245
71. Grunden, A. M., Jenney, F. E., Jr., Ma, K., Ji, M., Weinberg, M. V., and Adams, M. W. (2005) In vitro reconstitution of an NADPH-dependent superoxide reduction pathway from Pyrococcus furiosus. *Appl. Environ. Microbiol.* **71**, 1522–1530
72. Lee, H. J., Basran, J., and Scrutton, N. S. (1998) Electron transfer from flavin to iron in the Pseudomonas oleovorans rubredoxin reductase-rubredoxin electron transfer complex. *Biochemistry* **37**, 15513–15522
73. Gomes, C. M., Vicente, J. B., Wasserfallen, A., and Teixeira, M. (2000) Spectroscopic studies and characterization of a novel electron-transfer chain from Escherichia coli involving a flavorubredoxin and its flavoprotein reductase partner. *Biochemistry* **39**, 16230–16237